Journal of Advanced Ceramics
2021, **10**(3): 596–613
https://doi.org/10.1007/s40145-021-0461-6
ISSN 2226-4108
CN 10-1154/TQ

Research Article

Preparation and properties of CMAS resistant bixbyite structured high-entropy oxides RE_2O_3 (RE = Sm, Eu, Er, Lu, Y, and Yb): Promising environmental barrier coating materials for Al_2O_{3f}/Al_2O_3 composites

Yanan SUN[a,b], Huimin XIANG[b], Fu-Zhi DAI[b], Xiaohui WANG[c], Yan XING[d], Xiaojun ZHAO[a,*], Yanchun ZHOU[b,*]

[a]*School of Materials Science and Engineering, Central South University, Changsha 410083, China*
[b]*Science and Technology on Advanced Functional Composite Laboratory, Aerospace Research Institute of Materials & Processing Technology, Beijing 100076, China*
[c]*Shenyang National Laboratory for Materials Science, Institute of Metal Research, Chinese Academy of Sciences, Shenyang 110016, China*
[d]*New Energy Technology Engineering Laboratory of Jiangsu Province, Nanjing University of Posts and Telecommunications, Nanjing 210023, China*

Received: November 4, 2020; Revised: January 13, 2021; Accepted: January 17, 2021

Abstract: Y_2O_3 is regarded as one of the potential environmental barrier coating (EBC) materials for Al_2O_{3f}/Al_2O_3 ceramic matrix composites owing to its high melting point and close thermal expansion coefficient to Al_2O_3. However, the relatively high thermal conductivity and unsatisfactory calcium–magnesium–aluminosilicate (CMAS) resistance are the main obstacles for the practical application of Y_2O_3. In order to reduce the thermal conductivity and increase the CMAS resistance, four cubic bixbyite structured high-entropy oxides RE_2O_3, including $(Eu_{0.2}Er_{0.2}Lu_{0.2}Y_{0.2}Yb_{0.2})_2O_3$, $(Sm_{0.2}Er_{0.2}Lu_{0.2}Y_{0.2}Yb_{0.2})_2O_3$, $(Sm_{0.2}Eu_{0.2}Er_{0.2}Y_{0.2}Yb_{0.2})_2O_3$, and $(Sm_{0.2}Eu_{0.2}Lu_{0.2}Y_{0.2}Yb_{0.2})_2O_3$ were designed and synthesized, among which $(Eu_{0.2}Er_{0.2}Lu_{0.2}Y_{0.2}Yb_{0.2})_2O_3$ and $(Sm_{0.2}Er_{0.2}Lu_{0.2}Y_{0.2}Yb_{0.2})_2O_3$ bulks were prepared by spark plasma sintering (SPS) to investigate their mechanical and thermal properties as well as CMAS resistance. The mechanical properties of $(Eu_{0.2}Er_{0.2}Lu_{0.2}Y_{0.2}Yb_{0.2})_2O_3$ and $(Sm_{0.2}Er_{0.2}Lu_{0.2}Y_{0.2}Yb_{0.2})_2O_3$ are close to those of Y_2O_3 but become more brittle than Y_2O_3. The thermal conductivities of $(Eu_{0.2}Er_{0.2}Lu_{0.2}Y_{0.2}Yb_{0.2})_2O_3$ and $(Sm_{0.2}Er_{0.2}Lu_{0.2}Y_{0.2}Yb_{0.2})_2O_3$ (5.1 and 4.6 $W \cdot m^{-1} \cdot K^{-1}$) are only 23.8% and 21.5% respectively of that of Y_2O_3 (21.4 $W \cdot m^{-1} \cdot K^{-1}$), while their thermal expansion coefficients are close to those of Y_2O_3 and Al_2O_3. Most importantly, HE RE_2O_3 ceramics exhibit good CMAS resistance. After being attacked by CMAS at 1350 ℃ for 4 h, the HE RE_2O_3 ceramics maintain their original morphologies without forming pores or cracks, making them promising as EBC materials for Al_2O_{3f}/Al_2O_3 composites.

Keywords: high-entropy ceramics; rare earth oxides; low thermal conductivity; thermal expansion coefficient; CMAS resistance

* Corresponding authors.
E-mail: X. Zhao, Zhaoxj@csu.edu.cn;
Y. Zhou, yczhou@alum.imr.ac.cn

1 Introduction

Oxide/oxide ceramic matrix composites (CMCs) are promising materials for next generation gas turbine engines [1–6]. Among them, Al_2O_{3f}/Al_2O_3 composites are the up-to-date candidates but are restricted by their grain growth, sintering, creep deformation, water vapor recession [7–9], and CMAS corrosion [10–14] in combustion environment. To cope with the degradation problem, environmental barrier coatings (EBCs) have to be applied, which play an important role in protecting Al_2O_{3f}/Al_2O_3 composites from water vapor and CMAS attack.

Eligible EBC materials should have several fundamental but essential properties [15–17], i.e., (1) good high temperature phase stability without phase transition and decomposition, (2) good thermodynamic compatibility with substrates, (3) good mechanical strength and damage tolerance, (4) good resistance to water vapor and CMAS corrosion. Materials satisfying the foregoing requirements are potential as preeminent shields (EBCs) for Al_2O_{3f}/Al_2O_3 composites.

Previous works have demonstrated that Y_2O_3 is a potential EBC material because of its high melting point (2500 ℃) [18] and close thermal expansion coefficient ($(8.6–9.6)\times10^{-6}$ K^{-1}) [19,20] to Al_2O_3 ($(8.5–9.0)\times10^{-6}$ K^{-1}) [21]. However, the thermal conductivity of Y_2O_3 at room temperature is relatively high. Meanwhile, the CMAS resistance of Y_2O_3 is not as satisfactory as expected [22]. Therefore, reducing the thermal conductivity and improve CMAS resistance of Y_2O_3 is significant.

In the past few years, high-entropy ceramics (HECs) have been proven to have fascinating properties comparing to the single-component materials such as good stability, adjustable thermal expansion coefficient, low thermal conductivity, slow grain growth rate, high hardness and strength, and improved oxidation resistance [17,23–37]. Particularly, compositional disorder and severe lattice distortion can enhance phonon scattering, resulting in lower thermal conductivity. Moreover, improved corrosion resistance can be achieved due to sluggish diffusion.

In order to reduce the thermal conductivity and improve the CMAS resistance of Y_2O_3, four cubic bixbyite structured high-entropy rare earth oxides, i.e., $(Eu_{0.2}Er_{0.2}Lu_{0.2}Y_{0.2}Yb_{0.2})_2O_3$, $(Sm_{0.2}Er_{0.2}Lu_{0.2}Y_{0.2}Yb_{0.2})_2O_3$, $(Sm_{0.2}Eu_{0.2}Er_{0.2}Y_{0.2}Yb_{0.2})_2O_3$, and $(Sm_{0.2}Eu_{0.2}Lu_{0.2}Y_{0.2}Yb_{0.2})_2O_3$ were designed and synthesized in this work. When choosing the compositions, crystal structures and atomic differences were taken into account as the main criteria. Firstly, the constituting oxides are expected to crystallize in similar crystal structures. Secondly, the chosen five kinds of rare earth elements are supposed to have small ionic radius difference but high atomic mass difference. Thus, $(Eu_{0.2}Er_{0.2}Lu_{0.2}Y_{0.2}Yb_{0.2})_2O_3$ was designed as the initial composition, wherein five constituting oxides Eu_2O_3, Er_2O_3, Lu_2O_3, Y_2O_3, and Yb_2O_3 possess the same crystal structure. Then, in view of the fact that Sm_2O_3 has two types of crystal structures and its effect on the crystal structure of high-entropy rare earth oxides is unknown, by substituting Eu_2O_3, Er_2O_3, and Lu_2O_3 with Sm_2O_3 in order, the other three compositions, i.e., $(Sm_{0.2}Er_{0.2}Lu_{0.2}Y_{0.2}Yb_{0.2})_2O_3$, $(Sm_{0.2}Eu_{0.2}Er_{0.2}Y_{0.2}Yb_{0.2})_2O_3$, and $(Sm_{0.2}Eu_{0.2}Lu_{0.2}Y_{0.2}Yb_{0.2})_2O_3$ were designed.

The mechanisms underlying the low thermal conductivity of HECs are attributed to atomic mass difference and lattice distortion. For the electrical insulating HECs, the thermal conductivities are typically determined by a combination of phonon–phonon scattering and defect scattering [38]. The phonon relaxation time τ can be described as

$$\tau_{\mathrm{U}}(\omega)=\frac{(6\pi^2)^{1/3}}{2}\frac{\bar{M}\upsilon_{\mathrm{g}}\upsilon_{\mathrm{p}}^2}{k_{\mathrm{B}}V^{1/3}\gamma^2\omega^2T} \tag{1}$$

$$\tau_{\mathrm{PD}}^{-1}=\frac{V\omega^4}{4\pi\upsilon_{\mathrm{g}}\upsilon_{\mathrm{p}}^2}\left[\sum_i f_i\left(1-\frac{m_i}{\bar{m}}\right)^2+\sum_i f_i\left(1-\frac{r_i}{\bar{r}}\right)^2\right] \tag{2}$$

where τ_{U} and τ_{PD} refer to Umklapp phonon–phonon scattering and point defect scattering, respectively. In detail, $\bar{M}$ is the average mass, υ_{g} is the phonon group velocity, υ_{p} is the phonon phase velocity, V is the volume per atom, γ is the Grüneisen parameter, ω is the phonon frequency, f_i is the fraction of atoms with mass m_i and radius r_i on the site with average mass $\bar{m}$ and radius $\bar{r}$. Based on Eq. (1) and Eq. (2), it is reasonable to expect that the thermal conductivity of HE RE_2O_3 will be reduced compared to Y_2O_3 owing to big atomic mass difference and lattice distortion in HE RE_2O_3.

Aiming at reducing the thermal conductivity and improving the CMAS resistance of Y_2O_3, four cubic bixbyite structured high-entropy rare earth oxides, i.e., $(Eu_{0.2}Er_{0.2}Lu_{0.2}Y_{0.2}Yb_{0.2})_2O_3$, $(Sm_{0.2}Er_{0.2}Lu_{0.2}Y_{0.2}Yb_{0.2})_2O_3$, $(Sm_{0.2}Eu_{0.2}Er_{0.2}Y_{0.2}Yb_{0.2})_2O_3$, and $(Sm_{0.2}Eu_{0.2}Lu_{0.2}Y_{0.2}Yb_{0.2})_2O_3$ were designed, which have big atomic mass difference and ionic radius difference. These high-

entropy rare earth oxides were synthesized using Sm_2O_3, Eu_2O_3, Er_2O_3, Lu_2O_3, Y_2O_3, and Yb_2O_3 as starting materials, and then the mechanical and thermal properties as well as CMAS resistance were explored to assure their qualification as promising EBC materials for Al_2O_3f/Al_2O_3 composites.

2 Experimental

2. 1 Preparation and characterization of HE RE_2O_3 powders and bulks

Powders of $(Eu_{0.2}Er_{0.2}Lu_{0.2}Y_{0.2}Yb_{0.2})_2O_3$, $(Sm_{0.2}Er_{0.2}Lu_{0.2}Y_{0.2}Yb_{0.2})_2O_3$, $(Sm_{0.2}Eu_{0.2}Er_{0.2}Y_{0.2}Yb_{0.2})_2O_3$, and $(Sm_{0.2}Eu_{0.2}Lu_{0.2}Y_{0.2}Yb_{0.2})_2O_3$ were synthesized by the solid state reaction method. Five RE_2O_3 oxides chosen from six rare earth oxides, i.e., Y_2O_3, Sm_2O_3, Eu_2O_3, Er_2O_3, Yb_2O_3, and Lu_2O_3 powders (99.9% purity; HWRK Chem. Co., Ltd., Beijing, China) were mixed in equal molar ratios according to the above target compositions. The mixtures were cold pressed into pallets and then calcined at 1600 ℃ for 4 h in air. After cooling, these pallets were smashed and ball milled for 4 h to obtain fine powders.

Phase identification was performed by an X-ray diffractometer (XRD, D8 advanced, Bruker, Germany) using Cu Kα (λ =1.54178 Å) radiation at a scanning speed of 2 (°)/min. To prove that the as-prepared powders exhibit the cubic bixbyite structure, Rietveld refinement was conducted using TOPAS software (TOPAS, Bruker Corp., Karlsruhe, Germany). In Rietveld refinement, R factor is the sum of weighted and squared differences between observed and calculated intensities at each point in an XRD pattern which is minimized by least squares refinement as [39]:

$$R = \sum_i w_i \left| (y_i(\text{obs}) - y_i(\text{calc}) \right|^2 \quad (3)$$

where $y_i(\text{obs})$ and $y_i(\text{calc})$ are the observed and calculated intensities at point i respectively, w_i is the weight assigned to each intensity, and $y_i(\text{calc})$ can be calculated as follows:

$$y_i(\text{calc}) = S\sum_k (p_k L_k \left| F_k \right| G(\Delta\theta_{ik}) P_k) + y_i(\text{bkg}) \quad (4)$$

where S is a phase-specific scale factor, p_k is the multiplicity factor, L_k is the Lorentz and polarization factor for the kth Bragg reflection, F_k is the structure factor for an individual reflection of a particular phase, $G(\Delta\theta_{ik})$ is the reflection profile function, $\Delta\theta_{ik}$ is the Bragg angle for the kth reflection, P_k is the preferred orientation function, and $y_i(\text{bkg})$ is the refined background. In this way, reliability factors R_p [39] and R_wp [40] are built as

$$R_\text{p} = \frac{\sum \left| y_i(\text{obs}) - y_i(\text{calc}) \right|}{\sum y_i(\text{obs})} \quad (5)$$

$$R_\text{wp} = \left[\frac{\sum_i \dfrac{(y_i(\text{obs}) - y_i(\text{calc}))^2}{y_i(\text{obs})}}{\sum_i y_i(\text{obs})} \right]^{1/2} \quad (6)$$

wherein lower values indicate higher degree of agreements. The particle size distribution of HE RE_2O_3 powders was observed in a scanning electron microscope (SEM, Apollo300, CamScan, Cambrige, UK) and analyzed using ImageJ software (Open resource) [41] with at least 300 particles were counted.

Bulk HE RE_2O_3 ceramics were prepared by a spark plasma sintering apparatus (SPS-20T-6-IV, Shanghai Chenhua Science and Technology Co., Ltd., China) at 1500 ℃ for 10 min under a pressure of 30 MPa. The bulk density was measured by the Achimede's method. After being polished and thermally etched at 1500 ℃ for 1 h, microstructures and element distribution of HE RE_2O_3 ceramics were observed by a scanning electron microscope (SEM, Apollo300, CamScan, Cambridge, UK) equipped with energy dispersive X-ray spectroscopic system (EDS, Inca X-Max 80 T, Oxford, UK). The grain size distribution was analyzed using ImageJ software (open resource) [41] based on the microstructures of the thermally etched surface and at least 300 grains were counted.

2. 2 Mechanical properties of bulk HE RE_2O_3

Good mechanical properties and damage tolerance are basic requirements for EBC materials. To evaluate the suitability of HE RE_2O_3 as EBC materials, their mechanical properties were measured. For flexural strength and fracture toughness, at least five samples were tested using a universal testing machine (MTS-Criterio C45.105, USA). The flexural strength of HE RE_2O_3 was measured through a three-point bending test method with the sample dimension of 3 mm × 4 mm × 36 mm. Fracture toughness K_IC was determined using single-edge notched beam (SENB) specimens with the dimension of 3 mm × 6 mm × 36 mm. The

notch was 3 mm in depth and 0.15 mm in width. The crosshead speed for flexural strength test is 0.5 mm/min and that for K_{IC} determination is 0.05 mm/min. The elastic modulus E was estimated by a residual-indent analysis method. In this method, elastic modulus is a simple function of E_r [42]:

$$\frac{1}{E_r}=\frac{1-\nu^2}{E}+\frac{1-\nu_i^2}{E_i} \tag{7}$$

where E_r is the reduced modulus, E and v are the elastic modulus and Poisson's ratio of the specimen, while E_i and v_i are the elastic modulus and Poisson's ratio of the indenter, respectively.

2. 3 Thermal properties of bulk HE RE_2O_3

Thermal conductivity is one of the most important properties for HE RE_2O_3 that needs to make a breakthrough in this work. Thermal conductivity (κ) of HE RE_2O_3 can be calculated from thermal diffusivity (D_{th}), heat capacity (c_p), and bulk density (d) using:

$$\kappa = D_{th}\cdot c_p \cdot d \tag{8}$$

where c_p was calculated from the data of the constituent oxides (Y_2O_3, Sm_2O_3, Eu_2O_3, Er_2O_3, Yb_2O_3, and Lu_2O_3) by Neumann–Kopp rule. The thermal diffusivity (D_{th}) was measured by a laser flash thermal conductivity apparatus (NETZSCH LFA467, Germany). To achieve such a goal, samples with the size of Ø 10 mm × 2 mm were used and were coated by layers of platinum and graphite to prevent heat radiation from penetrating. The average linear thermal expansion coefficient (TEC) was obtained by a vertical high-temperature optical dilatometer (ODHT-1600-50, Expert System Solutions, Modena, Italy) from room temperature to 1673 K using a sample of 3 mm × 4 mm × 15 mm in size.

2. 4 CMAS resistance of HE RE_2O_3

Recently, CMAS corrosion has become a pending teaser which must be taking into consideration when developing EBC materials. To demonstrate the CMAS resistance of HE RE_2O_3 ceramics, a CMAS composition of $22CaO–19MgO–14AlO_{1.5}–45SiO_2$ [43] in molar ratio was used in this work. Firstly, homogeneous mixture of CaO, MgO, Al_2O_3, and SiO_2 powders were annealed at 1400 ℃ for 4 h to obtain CMAS powders. Secondly, by dispersing CMAS powders in ethanol, CMAS slurry was dropped on the polished surfaces of bulk HE RE_2O_3 ceramics with a loading density of about 77 mg/cm^2. After the evaporation of ethanol, the coated samples were heated to 1250 and 1350 ℃, respectively, for up to 4 h in a muffle furnace. Finally, the CMAS attacked samples were cut along their midline and the cross-sections were polished for SEM characterization.

3 Results and discussion

3. 1 Phase composition and microstructure of HE RE_2O_3 powders

Figure 1 shows the XRD patterns of HE RE_2O_3 powders and those of Y_2O_3, Sm_2O_3, Eu_2O_3, Er_2O_3, Yb_2O_3, and Lu_2O_3. One can see that although the XRD pattern of Sm_2O_3 is different from those of Y_2O_3, Eu_2O_3, Er_2O_3, Yb_2O_3, and Lu_2O_3, the XRD patterns of the four HE RE_2O_3 powders are similar to each other and coincide with those of cubic bixbyite structured RE_2O_3, indicating the formation of cubic bixbyite structured HE RE_2O_3.

Among the six selected rare earth oxides, Y_2O_3, Sm_2O_3, Eu_2O_3, Er_2O_3, Yb_2O_3, and Lu_2O_3 can all crystallize in cubic bixbyite structure. Nevertheless, the XRD patterns in Fig. 1 show that Y_2O_3, Eu_2O_3, Er_2O_3, Yb_2O_3, and Lu_2O_3 are in cubic bixbyite structure ($Ia\bar{3}$ space group) [44], while Sm_2O_3 is in monoclinic structure ($C2/m$ space group) [44,45]. Figures 2(a) and 2(b) show the crystal structure of cubic Y_2O_3 and that of monoclinic Sm_2O_3, respectively. Figure 2(c) shows the schematic crystal structure of high-entropy RE_2O_3, which was built based on a 2 × 2 × 2 supercell of Y_2O_3. In Y_2O_3, Y atoms are located at 8*a* (1/4, 1/4, 1/4) and 24*d* (*x*, 0, 1/4) sites, while O atoms occupy the 48*e* (*x*, *y*, *z*) site. In HE RE_2O_3, five kinds of RE atoms occupy the 8*a* and 24*d* sites randomly. Using the structure model of HE RE_2O_3 in Fig. 2(c), a simulated XRD pattern is obtained as shown in Fig. 2(d). This XRD pattern is very similar to those of cubic bixbyite oxides but with tiny peaks at low angle due to the supercell.

It has come to light that the stable crystal structure of the RE_2O_3 at room temperature varies with the atomic number of RE [46]. The light rare earth element oxides RE_2O_3, from La_2O_3 to Nd_2O_3, are stable in the form of hexagonal structure (A phase), while the middle rare earth element oxides RE_2O_3, including Sm_2O_3, Eu_2O_3, and Gd_2O_3, are stable in either monoclinic (B phase) or cubic structure (C phase). The heavy rare earth element oxides RE_2O_3, from Tb_2O_3 to

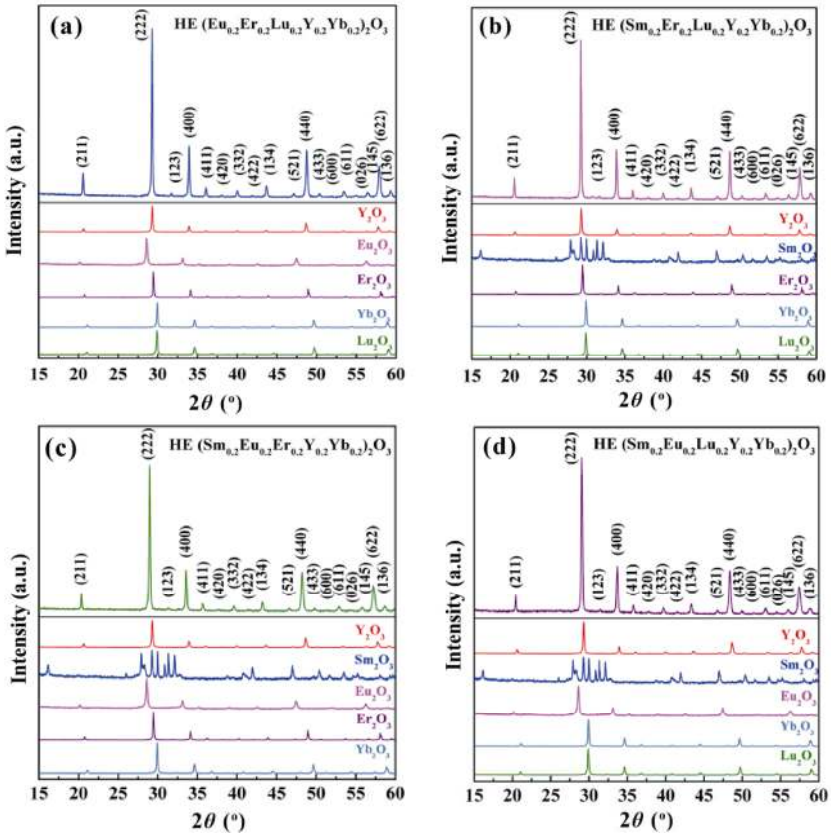

Fig. 1 XRD patterns of $(Eu_{0.2}Er_{0.2}Lu_{0.2}Y_{0.2}Yb_{0.2})_2O_3$, $(Sm_{0.2}Er_{0.2}Lu_{0.2}Y_{0.2}Yb_{0.2})_2O_3$, $(Sm_{0.2}Eu_{0.2}Er_{0.2}Y_{0.2}Yb_{0.2})_2O_3$, and $(Sm_{0.2}Eu_{0.2}Lu_{0.2}Y_{0.2}Yb_{0.2})_2O_3$ powders and those of the constituting oxides Y_2O_3, Sm_2O_3, Eu_2O_3, Er_2O_3, Yb_2O_3, and Lu_2O_3.

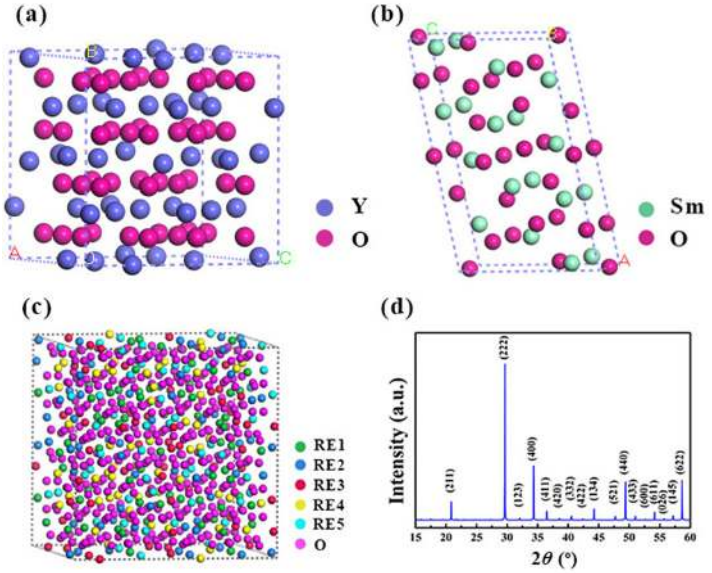

Fig. 2 Crystal structures of (a) cubic Y_2O_3, (b) monoclinic Sm_2O_3, (c) HE RE_2O_3, and (d) simulated XRD pattern of HE RE_2O_3.

Lu_2O_3, are stable only in cubic structure (C phase). In this work, HE RE_2O_3 powders are synthesized at 1600 ℃. Sm_2O_3 and Eu_2O_3 are supposed to transfer from cubic to monoclinic structure when the temperature reaches up to 1600 ℃. Theoretically, Sm_2O_3 and Eu_2O_3 obey an ideal transition sequence of cubic (C phase)→monoclinic (B phase)→hexagonal (A phase)→high temperature hexagonal (H phase)→high temperature cubic (X phase). The transition temperatures [46–52] are listed in Table 1.

Table 1 Phase transition temperatures of Sm_2O_3 and Eu_2O_3

Material	Transition temperature (℃)			
	C→B	B→A	A→H	H→X
Sm_2O_3	1153 [46]	2170 [46]	2369 [46]	2526 [46]
	1173–1273 [47]	2143 [48]	2403 [50]	2523 [50]
	1153 [49]	2173 [50]	2343 [48]	2498 [48]
Eu_2O_3	1348 [46]	2323 [46]	2413 [46]	2526 [46]
	1348 [47]	2323 [50]	2413 [50]	2523 [50]
	1323 [51]	2323 [52]	2413 [52]	2498 [48]

According to Table 1, the C→B phase transition temperatures of Sm_2O_3 and Eu_2O_3 are in a range of 1153–1348 ℃. The phase transition is irreversible [53]. XRD pattern of monoclinic structured Sm_2O_3 in ICSD database [54] and those of Sm_2O_3 before and after heated at 1600 ℃ for 4 h are shown in Fig. 3. Comparing with Fig. 1, after being heated at 1600 ℃ for 4 h, there was no phase transition for monoclinic structured Sm_2O_3. In HE RE_2O_3, however, monoclinic structured Sm_2O_3 has been dissolved into the cubic bixbyite structure. Since Sm_2O_3 has a different crystal structure, it demonstrates that materials with different crystal structures can be integrated into a homogeneous solid solution through entropy stabilization. In addition, cubic bixbyite structured Eu_2O_3 is supposed to transfer to a monoclinic structure after being heated at 1600 ℃ for 4 h. However, it remains in a cubic bixbyite structure in HE RE_2O_3. These facts demonstrate that the structural constraint of high-entropy oxides is effective in restraining phase transition and sustaining the phase stability [55].

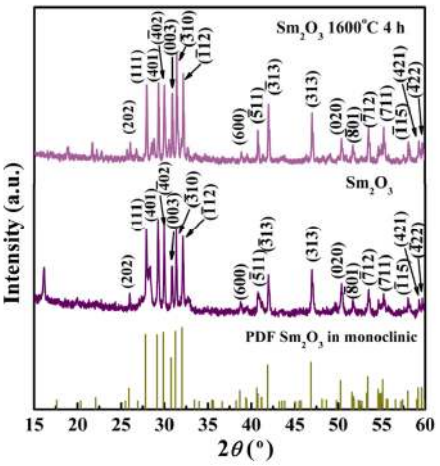

Fig. 3 XRD patterns of Sm_2O_3 before and after being heated at 1600 ℃ for 4 h together with peak positions and intensities in PDF#42-1464 of monoclinic structured Sm_2O_3 [54].

Lattice parameter a and theoretical density d_t of the four HE RE_2O_3, i.e., $(Eu_{0.2}Er_{0.2}Lu_{0.2}Y_{0.2}Yb_{0.2})_2O_3$, $(Sm_{0.2}Er_{0.2}Lu_{0.2}Y_{0.2}Yb_{0.2})_2O_3$, $(Sm_{0.2}Eu_{0.2}Er_{0.2}Y_{0.2}Yb_{0.2})_2O_3$, and $(Sm_{0.2}Eu_{0.2}Lu_{0.2}Y_{0.2}Yb_{0.2})_2O_3$ obtained by Rietveld refinement are listed in Table 2. The average lattice parameter a_{av} and density d_{av} of five constituting oxides are also included for comparison. Primarily, the R_p and R_{wp} values are less than 10, which indicate good reliability of the refinement. Analyzing of the data in the table, one can find that the refined lattice parameters a are somewhat smaller than the average lattice parameters a_{av}. And the theoretical densities d_t of HE RE_2O_3 are lower than the average densities of the constituting oxides d_{av}, from which the deviations are around 2%. From the above results, a conclusion can be drawn that for the HE RE_2O_3, the lattice parameters are not just the average of those the constituting components but are the results of energetic optimization of the structure after they reach thermodynamic equilibrium.

Interestingly, it should be pointed out that during the synthesis procedure, the solubility of $(Sm_{0.2}Eu_{0.2}Er_{0.2}Y_{0.2}Yb_{0.2})_2O_3$ and $(Sm_{0.2}Eu_{0.2}Lu_{0.2}Y_{0.2}Yb_{0.2})_2O_3$ powders changes over holding time. Figure 4 shows the XRD patterns of HE RE_2O_3 powders with different compositions heated for 1, 2, 3, and 4 h. As shown in Figs. 4(c) and 4(d), for $(Sm_{0.2}Eu_{0.2}Er_{0.2}Y_{0.2}Yb_{0.2})_2O_3$ and $(Sm_{0.2}Eu_{0.2}Lu_{0.2}Y_{0.2}Yb_{0.2})_2O_3$, wherein Sm and Eu co-exist, there are several weak peaks appearing on both sides of the strongest (222) peak compared with $(Eu_{0.2}Er_{0.2}Lu_{0.2}Y_{0.2}Yb_{0.2})_2O_3$ and $(Sm_{0.2}Er_{0.2}Lu_{0.2}Y_{0.2}Yb_{0.2})_2O_3$ powders after 1 h heating. With the extension of heating time to 2 and 3 h, these peaks are weakened. XRD patterns of the four specimens that are heated for 4 h converge with each other eventually. Time dependent peak change may be caused by atomic size differences, which results in time dependent solubilities. Sm and Eu are the two largest atoms of the selected rare earth elements with the ionic radii of 0.964 and 0.950 Å [56], respectively, as summarized in Table 3. This fact implies that it takes more time for big atoms to incorporate into a homogeneous solid solution. In terms of the time-independent solubility of $(Eu_{0.2}Er_{0.2}Lu_{0.2}Y_{0.2}Yb_{0.2})_2O_3$ and $(Sm_{0.2}Er_{0.2}Lu_{0.2}Y_{0.2}Yb_{0.2})_2O_3$ at 1600 ℃, $(Eu_{0.2}Er_{0.2}Lu_{0.2}Y_{0.2}Yb_{0.2})_2O_3$ has the biggest relative atomic mass difference among the four HE RE_2O_3, while $(Sm_{0.2}Er_{0.2}Lu_{0.2}Y_{0.2}Yb_{0.2})_2O_3$ has the biggest ionic radii difference. Thus, $(Eu_{0.2}Er_{0.2}Lu_{0.2}Y_{0.2}Yb_{0.2})_2O_3$ and $(Sm_{0.2}Er_{0.2}Lu_{0.2}Y_{0.2}Yb_{0.2})_2O_3$ are consolidated into bulk form and investigated deeply in this work as representatives.

Table 2 Lattice parameters and densities of $(Eu_{0.2}Er_{0.2}Lu_{0.2}Y_{0.2}Yb_{0.2})_2O_3$, $(Sm_{0.2}Er_{0.2}Lu_{0.2}Y_{0.2}Yb_{0.2})_2O_3$, $(Sm_{0.2}Eu_{0.2}Er_{0.2}Y_{0.2}Yb_{0.2})_2O_3$, and $(Sm_{0.2}Eu_{0.2}Lu_{0.2}Y_{0.2}Yb_{0.2})_2O_3$

Material	a (Å)	a_{av} (Å)	V (Å^3)	d_t (g/cm^3)	d_{av} (g/cm^3)	R_p	R_{wp}
$(Eu_{0.2}Er_{0.2}Lu_{0.2}Yb_{0.2}Y_{0.2})_2O_3$	10.563	10.569	1178.586	7.899	7.944	4.90	6.22
$(Sm_{0.2}Er_{0.2}Lu_{0.2}Yb_{0.2}Y_{0.2})_2O_3$	10.575	10.583	1182.609	7.854	8.038	4.95	6.23
$(Sm_{0.2}Eu_{0.2}Er_{0.2}Yb_{0.2}Y_{0.2})_2O_3$	10.666	10.681	1213.402	7.453	7.590	4.90	6.69
$(Sm_{0.2}Eu_{0.2}Lu_{0.2}Yb_{0.2}Y_{0.2})_2O_3$	10.636	10.646	1203.192	7.587	7.762	6.71	8.91

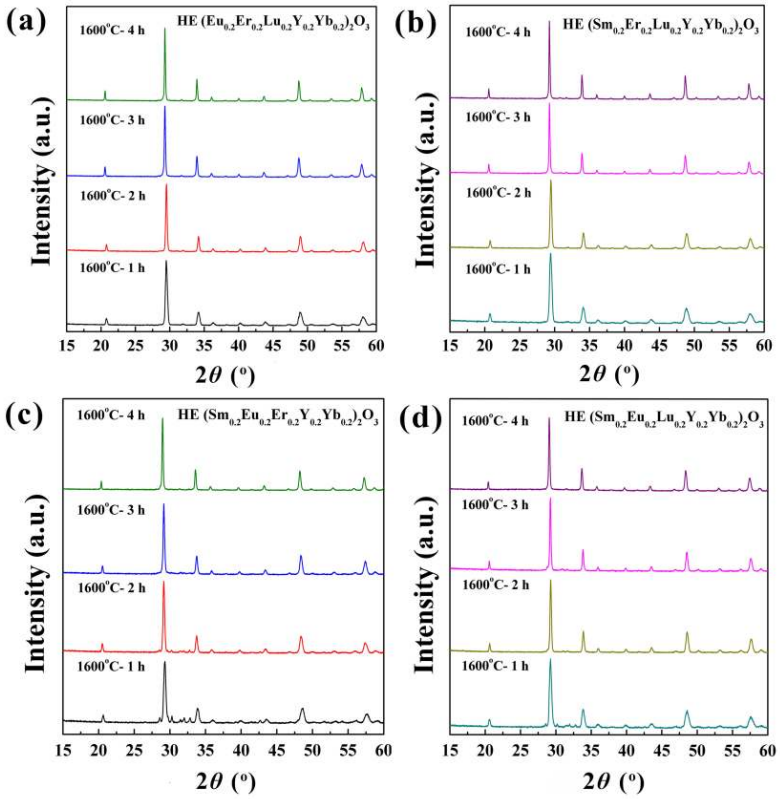

Fig. 4 XRD patterns of the as-prepared $(Eu_{0.2}Er_{0.2}Lu_{0.2}Y_{0.2}Yb_{0.2})_2O_3$, $(Sm_{0.2}Er_{0.2}Lu_{0.2}Y_{0.2}Yb_{0.2})_2O_3$, $(Sm_{0.2}Eu_{0.2}Er_{0.2}Y_{0.2}Yb_{0.2})_2O_3$, and $(Sm_{0.2}Eu_{0.2}Lu_{0.2}Y_{0.2}Yb_{0.2})_2O_3$ powders synthesized at 1600 ℃ from 1 to 4 h.

Table 3 Atomic and ionic radii, relative atomic mass, and the relative ionic radius differences of the selected rare earth elements

Element	Atomic radius (Å) [56]	Ionic radius RE^{3+} (Å) [56]	Coordination number	Ionic radius difference	Mass (g/mol)	Mass difference
Sm	1.814	0.964	6	13.7%	150	68.5%
Eu	1.984	0.950	6	12.0%	152	70.8%
Er	1.780	0.881	6	3.9%	167	87.6%
Yb	1.923	0.858	6	1.2%	173	94.4%
Lu	1.760	0.848	6	0	175	96.6%
Y	1.824	0.892	6	5.2%	89	0

SEM images of $(Eu_{0.2}Er_{0.2}Lu_{0.2}Y_{0.2}Yb_{0.2})_2O_3$ and $(Sm_{0.2}Er_{0.2}Lu_{0.2}Y_{0.2}Yb_{0.2})_2O_3$ powders and the corresponding statistics of particle size are shown in Fig. 5. It can be seen from Figs. 5(a) and 5(c) that the particle sizes of $(Eu_{0.2}Er_{0.2}Lu_{0.2}Y_{0.2}Yb_{0.2})_2O_3$ and $(Sm_{0.2}Er_{0.2}Lu_{0.2}Y_{0.2}Yb_{0.2})_2O_3$ are analogous. Following a log-normal distribution in Figs. 5(b) and 5(d), the average particle sizes of $(Eu_{0.2}Er_{0.2}Lu_{0.2}Y_{0.2}Yb_{0.2})_2O_3$ and $(Sm_{0.2}Er_{0.2}Lu_{0.2}Y_{0.2}Yb_{0.2})_2O_3$ are determined 1.09±0.53 and 1.35±0.62 μm, respectively.

3.2 Phase composition and microstructure of bulk $(Eu_{0.2}Er_{0.2}Lu_{0.2}Y_{0.2}Yb_{0.2})_2O_3$ and $(Sm_{0.2}Er_{0.2}Lu_{0.2}Y_{0.2}Yb_{0.2})_2O_3$ ceramics

Bulk $(Eu_{0.2}Er_{0.2}Lu_{0.2}Y_{0.2}Yb_{0.2})_2O_3$ and $(Sm_{0.2}Er_{0.2}Lu_{0.2}Y_{0.2}Yb_{0.2})_2O_3$ ceramics were prepared by spark plasma sintering at 1500 ℃ under a pressure of 30 MPa for 10 min. For comparison, bulk Y_2O_3, which was used to obtain its thermal conductivity, was sintered under the same condition. XRD patterns of the three bulks are shown in Fig. 6. For both $(Eu_{0.2}Er_{0.2}Lu_{0.2}Y_{0.2}Yb_{0.2})_2O_3$ and

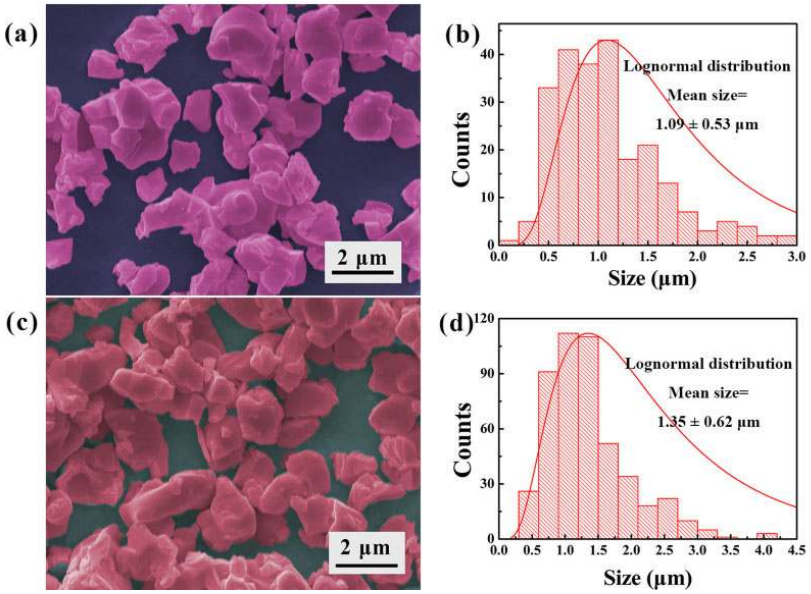

Fig. 5 Particle morphologies (a, c) and particle size distributions (b, d) of $(Eu_{0.2}Er_{0.2}Lu_{0.2}Y_{0.2}Yb_{0.2})_2O_3$ and $(Sm_{0.2}Er_{0.2}Lu_{0.2}Y_{0.2}Yb_{0.2})_2O_3$ powders.

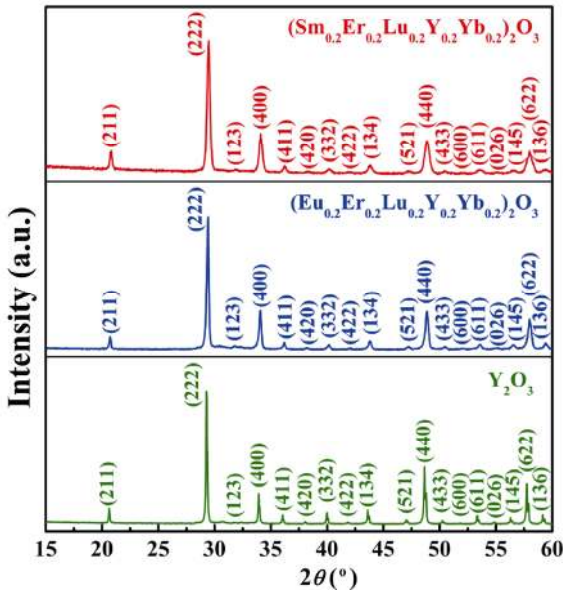

Fig. 6 XRD patterns of bulk $(Eu_{0.2}Er_{0.2}Lu_{0.2}Y_{0.2}Yb_{0.2})_2O_3$, $(Sm_{0.2}Er_{0.2}Lu_{0.2}Y_{0.2}Yb_{0.2})_2O_3$, and Y_2O_3.

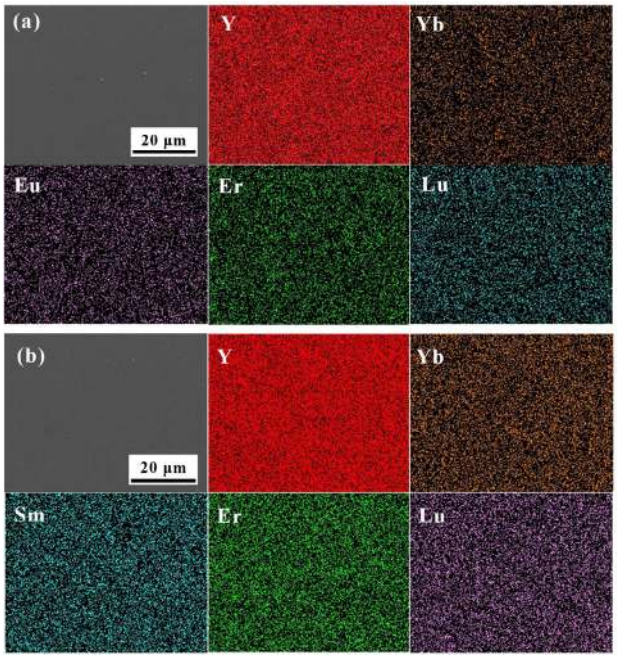

Fig. 7 Surfaces of the polished (a) $(Eu_{0.2}Er_{0.2}Lu_{0.2}Y_{0.2}Yb_{0.2})_2O_3$, (b) $(Sm_{0.2}Er_{0.2}Lu_{0.2}Y_{0.2}Yb_{0.2})_2O_3$, and the EDS mappings of the constituting rare earth elements.

$(Sm_{0.2}Er_{0.2}Lu_{0.2}Y_{0.2}Yb_{0.2})_2O_3$, no impurity phase can be identified within the resolution of X-ray diffraction, indicating high phase purity and good high temperature stability of high-entropy $(Eu_{0.2}Er_{0.2}Lu_{0.2}Y_{0.2}Yb_{0.2})_2O_3$ and $(Sm_{0.2}Er_{0.2}Lu_{0.2}Y_{0.2}Yb_{0.2})_2O_3$.

The densities of bulk $(Eu_{0.2}Er_{0.2}Lu_{0.2}Y_{0.2}Yb_{0.2})_2O_3$, $(Sm_{0.2}Er_{0.2}Lu_{0.2}Y_{0.2}Yb_{0.2})_2O_3$, and Y_2O_3 measured by Archimede's method are 7.88, 7.82, and 5.03 g/cm^3, respectively, corresponding to 99.8%, 99.6%, and 99.9% of the theoretical values. Figure 7 shows the SEM images of the polished surfaces of bulk $(Eu_{0.2}Er_{0.2}Lu_{0.2}Y_{0.2}Yb_{0.2})_2O_3$, $(Sm_{0.2}Er_{0.2}Lu_{0.2}Y_{0.2}Yb_{0.2})_2O_3$ and the distribution of constituting elements. Apparently, there are no micro-pores or micro-cracks in the observed region, revealing high density of the bulk HE RE_2O_3 ceramics. Moreover, it also can be seen from the figure that the corresponding rare earth elements are uniformly distributed in both bulk $(Eu_{0.2}Er_{0.2}Lu_{0.2}$

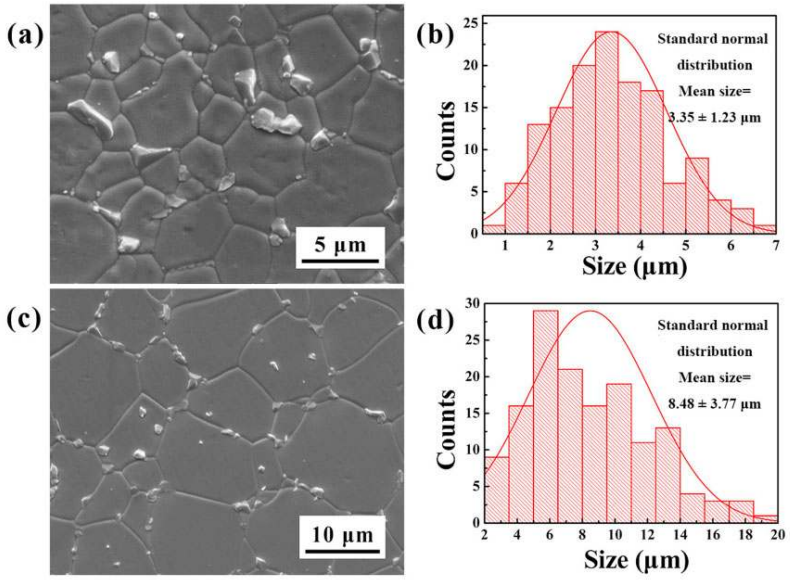

Fig. 8 SEM images of the microstructures (a, c) and grain size distributions (b, d) of bulk $(Eu_{0.2}Er_{0.2}Lu_{0.2}Y_{0.2}Yb_{0.2})_2O_3$ and $(Sm_{0.2}Er_{0.2}Lu_{0.2}Y_{0.2}Yb_{0.2})_2O_3$ thermally etched at 1500 ℃ for 1 h.

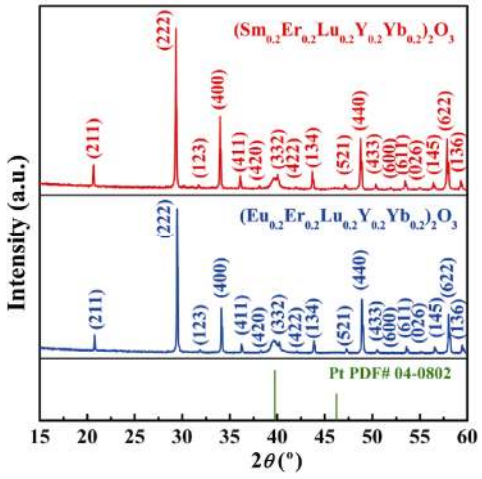

Fig. 9 XRD patterns of the thermally etched $(Eu_{0.2}Er_{0.2}Lu_{0.2}Y_{0.2}Yb_{0.2})_2O_3$ and $(Sm_{0.2}Er_{0.2}Lu_{0.2}Y_{0.2}Yb_{0.2})_2O_3$.

$Y_{0.2}Yb_{0.2})_2O_3$ and bulk $(Sm_{0.2}Er_{0.2}Lu_{0.2}Y_{0.2}Yb_{0.2})_2O_3$.

Figure 8 shows the surface microstructures and grain size distributions of bulk $(Eu_{0.2}Er_{0.2}Lu_{0.2}Y_{0.2}Yb_{0.2})_2O_3$ and $(Sm_{0.2}Er_{0.2}Lu_{0.2}Y_{0.2}Yb_{0.2})_2O_3$, which were thermally etched at 1500 ℃ for 1 h. No residual cracks or pores are in sight, whereas the average grain size of $(Eu_{0.2}Er_{0.2}Lu_{0.2}Y_{0.2}Yb_{0.2})_2O_3$ is less than half of that of $(Sm_{0.2}Er_{0.2}Lu_{0.2}Y_{0.2}Yb_{0.2})_2O_3$. The mean grain sizes of $(Eu_{0.2}Er_{0.2}Lu_{0.2}Y_{0.2}Yb_{0.2})_2O_3$ and $(Sm_{0.2}Er_{0.2}Lu_{0.2}Y_{0.2}Yb_{0.2})_2O_3$ are 3.55±1.23 and 8.48±3.77 μm, respectively. X-ray diffraction patterns from surfaces of the thermally etched $(Eu_{0.2}Er_{0.2}Lu_{0.2}Y_{0.2}Yb_{0.2})_2O_3$ and $(Sm_{0.2}Er_{0.2}Lu_{0.2}Y_{0.2}Yb_{0.2})_2O_3$ indicate no phase transition, as shown in Fig. 9. The XRD patterns of the thermally etched $(Eu_{0.2}Er_{0.2}Lu_{0.2}Y_{0.2}Yb_{0.2})_2O_3$ and $(Sm_{0.2}Er_{0.2}Lu_{0.2}Y_{0.2}Yb_{0.2})_2O_3$ are consistent with the original patterns of bulk $(Eu_{0.2}Er_{0.2}Lu_{0.2}Y_{0.2}Yb_{0.2})_2O_3$ and $(Sm_{0.2}Er_{0.2}Lu_{0.2}Y_{0.2}Yb_{0.2})_2O_3$, conforming the good high temperature stability of HE RE_2O_3 ceramics. Besides, the bulge peaks on the left side of (332) are identified to be platinum that wrapped the samples to improve their electrical conductivity before SEM observation.

3.3 Mechanical properties of $(Eu_{0.2}Er_{0.2}Lu_{0.2}Y_{0.2}Yb_{0.2})_2O_3$ and $(Sm_{0.2}Er_{0.2}Lu_{0.2}Y_{0.2}Yb_{0.2})_2O_3$

Mechanical properties, including Young's modulus E, fracture toughness K_{IC}, flexural strength σ_b, and Vickers hardness H_v of bulk $(Eu_{0.2}Er_{0.2}Lu_{0.2}Y_{0.2}Yb_{0.2})_2O_3$ and $(Sm_{0.2}Er_{0.2}Lu_{0.2}Y_{0.2}Yb_{0.2})_2O_3$ are summarized in Table 4. For comparison, the mechanical properties of Y_2O_3 [57] are also given. The Young's moduli measured by residual indent method are 205±10.1 and 189±3.7 GPa for $(Eu_{0.2}Er_{0.2}Lu_{0.2}Y_{0.2}Yb_{0.2})_2O_3$ and $(Sm_{0.2}Er_{0.2}Lu_{0.2}Y_{0.2}Yb_{0.2})_2O_3$, respectively, which are higher than that of Y_2O_3 (181.4 GPa). The higher Young's modulus can be understood from the difference in lattice parameters a of $(Eu_{0.2}Er_{0.2}Lu_{0.2}Y_{0.2}Yb_{0.2})_2O_3$ (10.563 Å), $(Sm_{0.2}Er_{0.2}Lu_{0.2}Y_{0.2}Yb_{0.2})_2O_3$ (10.567 Å), and Y_2O_3 (10.604 Å) [44] as shown in Table 2. Smaller lattice parameters of $(Eu_{0.2}Er_{0.2}Lu_{0.2}Y_{0.2}Yb_{0.2})_2O_3$ and $(Sm_{0.2}Er_{0.2}Lu_{0.2}Y_{0.2}Yb_{0.2})_2O_3$ indicate stronger bonding, which in turn lead to their slightly higher Young's modulus than Y_2O_3.

Table 4 Young's modulus E, fracture toughness K_{IC}, flexural strength σ_b, Vickers hardness H_v, damage tolerance D_t, and brittleness B of bulk $(Eu_{0.2}Er_{0.2}Lu_{0.2}Y_{0.2}Yb_{0.2})_2O_3$, $(Sm_{0.2}Er_{0.2}Lu_{0.2}Y_{0.2}Yb_{0.2})_2O_3$, and Y_2O_3

Material	E (GPa)	K_{IC} (MPa·m$^{1/2}$)	σ_b (MPa)	H_v (GPa)	D_t (m$^{1/2}$)	B (μm$^{-1/2}$)
$(Eu_{0.2}Er_{0.2}Lu_{0.2}Y_{0.2}Yb_{0.2})_2O_3$	205±10.1	1.67±0.13	165.7±0.57	7.55±0.04	0.254	4.521
$(Sm_{0.2}Er_{0.2}Lu_{0.2}Y_{0.2}Yb_{0.2})_2O_3$	189±3.7	1.64±0.11	166.1±5.37	7.42±0.24	0.233	4.524
Y_2O_3 [55]	181.4	2.06	122	7.60	0.374	3.689

The measured room temperature fracture toughness of bulk $(Eu_{0.2}Er_{0.2}Lu_{0.2}Y_{0.2}Yb_{0.2})_2O_3$ and $(Sm_{0.2}Er_{0.2}Lu_{0.2}Y_{0.2}Yb_{0.2})_2O_3$ are 1.67±0.13 and 1.64±0.11 MPa·m$^{1/2}$, respectively, which are lower than that of Y_2O_3 (2.06 MPa·m$^{1/2}$). The flexural strengths of $(Eu_{0.2}Er_{0.2}Lu_{0.2}Y_{0.2}Yb_{0.2})_2O_3$ and $(Sm_{0.2}Er_{0.2}Lu_{0.2}Y_{0.2}Yb_{0.2})_2O_3$ are 165.7±0.57 and 166.1±5.37 MPa, respectively, which are higher than that of Y_2O_3 (122 MPa). Lower fracture toughness and higher flexural strength than Y_2O_3 indicate that $(Eu_{0.2}Er_{0.2}Lu_{0.2}Y_{0.2}Yb_{0.2})_2O_3$ and $(Sm_{0.2}Er_{0.2}Lu_{0.2}Y_{0.2}Yb_{0.2})_2O_3$ are more brittle. The Vickers hardness of $(Eu_{0.2}Er_{0.2}Lu_{0.2}Y_{0.2}Yb_{0.2})_2O_3$ and $(Sm_{0.2}Er_{0.2}Lu_{0.2}Y_{0.2}Yb_{0.2})_2O_3$ are 7.55±0.04 and 7.42±0.24 GPa, which are close to that of Y_2O_3 (7.60 GPa). Brittleness index [58] in Eq. (9):

$$B = \frac{H}{K_{IC}} \tag{9}$$

and damage tolerance expressed in Eq. (10) [59]:

$$D_t = \frac{K_{IC} \cdot E}{\sigma_b \cdot H} \tag{10}$$

are quantitative measure of brittleness and damage tolerance, respectively. The values of brittleness of $(Eu_{0.2}Er_{0.2}Lu_{0.2}Y_{0.2}Yb_{0.2})_2O_3$ and $(Sm_{0.2}Er_{0.2}Lu_{0.2}Y_{0.2}Yb_{0.2})_2O_3$ are 4.521 and 4.524 μm$^{-1/2}$, respectively, which are higher than that of Y_2O_3 (3.689 μm$^{-1/2}$). The values of damage tolerance of $(Eu_{0.2}Er_{0.2}Lu_{0.2}Y_{0.2}Yb_{0.2})_2O_3$ and $(Sm_{0.2}Er_{0.2}Lu_{0.2}Y_{0.2}Yb_{0.2})_2O_3$ are 0.254 and 0.233 m$^{1/2}$, which are lower than that of Y_2O_3 (0.374 m$^{1/2}$). The relatively high brittleness and low damage tolerance values of $(Eu_{0.2}Er_{0.2}Lu_{0.2}Y_{0.2}Yb_{0.2})_2O_3$ and $(Sm_{0.2}Er_{0.2}Lu_{0.2}Y_{0.2}Yb_{0.2})_2O_3$ imply that $(Eu_{0.2}Er_{0.2}Lu_{0.2}Y_{0.2}Yb_{0.2})_2O_3$ and $(Sm_{0.2}Er_{0.2}Lu_{0.2}Y_{0.2}Yb_{0.2})_2O_3$ are more brittle than Y_2O_3. Although the damage tolerances D_t of $(Eu_{0.2}Er_{0.2}Lu_{0.2}Y_{0.2}Yb_{0.2})_2O_3$ and $(Sm_{0.2}Er_{0.2}Lu_{0.2}Y_{0.2}Yb_{0.2})_2O_3$ are lower than Y_2O_3, they are still close to that of $Y_4Al_2O_9$ (0.25 m$^{1/2}$), a candidate thermal barrier coating material [60], which still warrant their resistance to damage.

Figure 10 compares the fracture surfaces of $(Eu_{0.2}Er_{0.2}Lu_{0.2}Y_{0.2}Yb_{0.2})_2O_3$ and $(Sm_{0.2}Er_{0.2}Lu_{0.2}Y_{0.2}Yb_{0.2})_2O_3$

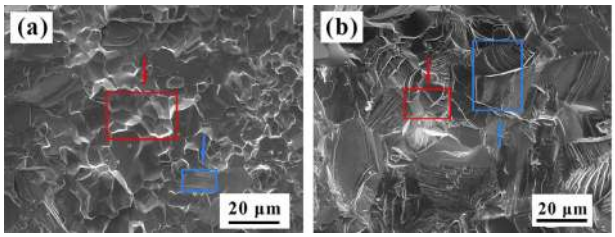

Fig. 10 Fracture surfaces of (a) $(Eu_{0.2}Er_{0.2}Lu_{0.2}Y_{0.2}Yb_{0.2})_2O_3$ and (b) $(Sm_{0.2}Er_{0.2}Lu_{0.2}Y_{0.2}Yb_{0.2})_2O_3$ (blue arrows indicate characteristic zone of intragranular fracture, while red arrows indicate characteristic zone of intergranular fracture).

after fracture toughness test. It can be seen that both of the fracture surfaces exhibit a combination of intragranular fracture (blue arrows indicate region) and intergranular fracture (red arrows indicate region). In Fig. 10(a), intact grain boundaries can clearly be seen, which signify that intergranular fracture occurs primarily in $(Eu_{0.2}Er_{0.2}Lu_{0.2}Y_{0.2}Yb_{0.2})_2O_3$. On the contrary, cleavage steps caused by crack penetration inside the grains exist mainly in Fig. 10(b), which promotes the dissipation of fracture energy. The difference between fracture surfaces of $(Eu_{0.2}Er_{0.2}Lu_{0.2}Y_{0.2}Yb_{0.2})_2O_3$ and $(Sm_{0.2}Er_{0.2}Lu_{0.2}Y_{0.2}Yb_{0.2})_2O_3$ is the result of grain size difference. The average grain size of $(Sm_{0.2}Er_{0.2}Lu_{0.2}Y_{0.2}Yb_{0.2})_2O_3$ is 8.48±3.77 μm, which is more than twice of that of $(Eu_{0.2}Er_{0.2}Lu_{0.2}Y_{0.2}Yb_{0.2})_2O_3$ (3.35±1.23 μm). When fracture occurs, cracks have to extend across the interior of grains in $(Sm_{0.2}Er_{0.2}Lu_{0.2}Y_{0.2}Yb_{0.2})_2O_3$, forming cleavage steps.

3.4 Thermal properties of $(Eu_{0.2}Er_{0.2}Lu_{0.2}Y_{0.2}Yb_{0.2})_2O_3$ and $(Sm_{0.2}Er_{0.2}Lu_{0.2}Y_{0.2}Yb_{0.2})_2O_3$

Thermal properties are key parameters to judge the qualification of $(Eu_{0.2}Er_{0.2}Lu_{0.2}Y_{0.2}Yb_{0.2})_2O_3$ and $(Sm_{0.2}Er_{0.2}Lu_{0.2}Y_{0.2}Yb_{0.2})_2O_3$ as EBC materials. The linear thermal expansion curves of $(Eu_{0.2}Er_{0.2}Lu_{0.2}Y_{0.2}Yb_{0.2})_2O_3$ and $(Sm_{0.2}Er_{0.2}Lu_{0.2}Y_{0.2}Yb_{0.2})_2O_3$ measured from room temperature to 1673 K are shown in Fig. 11. Distinctly, the expansion of samples increases linearly with temperature without excessive fluctuation caused by phase transition or decomposition, which also

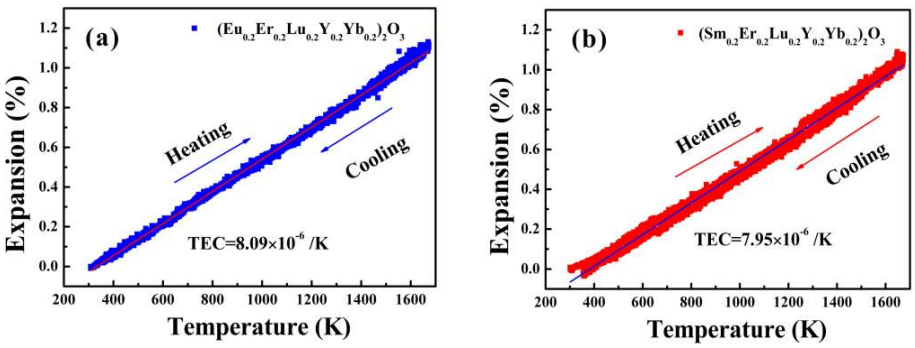

Fig. 11 Thermal expansion curves of $(Eu_{0.2}Er_{0.2}Lu_{0.2}Y_{0.2}Yb_{0.2})_2O_3$ and $(Sm_{0.2}Er_{0.2}Lu_{0.2}Y_{0.2}Yb_{0.2})_2O_3$ measured from room temperature to 1673 K.

proves the good high temperature stability of $(Eu_{0.2}Er_{0.2}Lu_{0.2}Y_{0.2}Yb_{0.2})_2O_3$ and $(Sm_{0.2}Er_{0.2}Lu_{0.2}Y_{0.2}Yb_{0.2})_2O_3$ in the testing temperature range. As shown in Figs. 11(a) and 11(b), the thermal expansion coefficients of $(Eu_{0.2}Er_{0.2}Lu_{0.2}Y_{0.2}Yb_{0.2})_2O_3$ and $(Sm_{0.2}Er_{0.2}Lu_{0.2}Y_{0.2}Yb_{0.2})_2O_3$ determined by linear fitting are 8.09×10^{-6} K^{-1} (R^2 = 0.997) and 7.95×10^{-6} K^{-1} (R^2 = 0.993), respectively, which are close to those of Y_2O_3 ((8.6–9.6)×10^{-6} K^{-1}) [19,20] and Al_2O_3 ((8.5–9.0)×10^{-6} K^{-1}) [21]. The difference between TECs of $(Eu_{0.2}Er_{0.2}Lu_{0.2}Y_{0.2}Yb_{0.2})_2O_3$ and $(Sm_{0.2}Er_{0.2}Lu_{0.2}Y_{0.2}Yb_{0.2})_2O_3$ may result from the difference of their chemical bonding [58,61].

Table 5 compares the thermal expansion coefficients (TECs) of the selected cubic bixbyite structured rare earth oxides [53]. In general, the TECs of HE RE_2O_3 are slightly smaller than those of single component rare earth oxides, which distribute in a range of (8.2–8.9)×10^{-6} K^{-1}. This fact implies that the TECs of HE RE_2O_3 stem from complex synergism of the component rare earth oxides instead of the average of them. Basically, thermal expansion of materials originates from anharmonic vibration of lattice at finite temperatures, which is closely related to the bond strength of chemical bond. Since the TECs of HE RE_2O_3 are smaller than those of the constituting rare earth oxides, the RE–O bonds in HE RE_2O_3 are statistically stronger than the RE–O bonds in single phase RE_2O_3. The enhanced Young's modulus of HE RE_2O_3 is a clear indication of stronger bonding than in the single component rare earth oxides RE_2O_3 since it is a direct reflection of chemical bonding.

Table 5 Thermal expansion coefficients of the selected cubic bixbyite structured rare earth oxides in different temperature ranges [53]

Material	Temperature range (℃)	TEC (10^{-6} K^{-1})
Y_2O_3	0–1400	8.2
	500–1400	8.9
Sm_2O_3	0–950	8.8
Eu_2O_3	0–1261	8.5
Er_2O_3	0–1312	8.4
Yb_2O_3	0–1293	8.4
Lu_2O_3	0–1300	8.2

The measured thermal diffusivities D_{th}, calculated heat capacities c_p, and the room temperature thermal conductivities κ of HE RE_2O_3 and Y_2O_3 are listed in Table 6. The room temperature thermal diffusivities of $(Eu_{0.2}Er_{0.2}Lu_{0.2}Y_{0.2}Yb_{0.2})_2O_3$ and $(Sm_{0.2}Er_{0.2}Lu_{0.2}Y_{0.2}Yb_{0.2})_2O_3$ are 1.92×10^{-6} and 1.88×10^{-6} $m^2\cdot s^{-1}$, respectively. And the room temperature thermal conductivities

Table 6 Room temperature thermal diffusivities D_{th}, heat capacities c_p, and thermal conductivities κ of HE RE_2O_3 and Y_2O_3

Material	D_{th} (10^{-6} $m^2\cdot s^{-1}$)	c_p ($J\cdot mol^{-1}\cdot K^{-1}$)	κ ($W\cdot m^{-1}\cdot K^{-1}$)
$(Eu_{0.2}Er_{0.2}Lu_{0.2}Y_{0.2}Yb_{0.2})_2O_3$	1.92	109.55	5.1
$(Sm_{0.2}Er_{0.2}Lu_{0.2}Y_{0.2}Yb_{0.2})_2O_3$	1.88	108.19	4.6
Y_2O_3	5.23	102.32	21.4

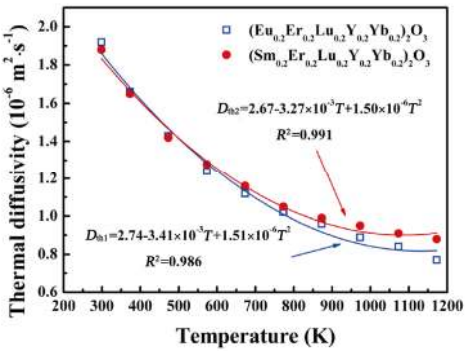

Fig. 12 Thermal diffusivities of $(Eu_{0.2}Er_{0.2}Lu_{0.2}Y_{0.2}Yb_{0.2})_2O_3$ and $(Sm_{0.2}Er_{0.2}Lu_{0.2}Y_{0.2}Yb_{0.2})_2O_3$ measured from room temperature to 1173 K.

of $(Eu_{0.2}Er_{0.2}Lu_{0.2}Y_{0.2}Yb_{0.2})_2O_3$ and $(Sm_{0.2}Er_{0.2}Lu_{0.2}Y_{0.2}Yb_{0.2})_2O_3$ are 5.1 and 4.6 $W\cdot m^{-1}\cdot K^{-1}$, respectively. One can see that the thermal diffusivities and thermal conductivities of HE RE_2O_3 are much lower than those of Y_2O_3 (5.23×10^{-6} $m^2\cdot s^{-1}$ and 21.4 $W\cdot m^{-1}\cdot K^{-1}$). Figure 12 shows the thermal diffusivities measured from room temperature to 1173 K. Curve fitting of the scatters of $(Eu_{0.2}Er_{0.2}Lu_{0.2}Y_{0.2}Yb_{0.2})_2O_3$ and $(Sm_{0.2}Er_{0.2}Lu_{0.2}Y_{0.2}Yb_{0.2})_2O_3$ yields:

$$D_{th1} = 2.74 - 3.41\times10^{-3}T + 1.51\times10^{-6}T^2 \quad \text{for } (Eu_{0.2}Er_{0.2}Lu_{0.2}Y_{0.2}Yb_{0.2})_2O_3 \tag{10}$$

$$D_{th2} = 2.67 - 3.27\times10^{-3}T + 1.50\times10^{-6}T^2 \quad \text{for } (Sm_{0.2}Er_{0.2}Lu_{0.2}Y_{0.2}Yb_{0.2})_2O_3 \tag{11}$$

wherein R^2 is 0.986 and 0.991 respectively. Heat capacities c_{p1} and c_{p2} as functions of temperature for $(Eu_{0.2}Er_{0.2}Lu_{0.2}Y_{0.2}Yb_{0.2})_2O_3$ and $(Sm_{0.2}Er_{0.2}Lu_{0.2}Y_{0.2}Yb_{0.2})_2O_3$) calculated by Neumann–Kopp rule yield (as shown in Fig. 13):

$$c_{p1} = 122.72 + 14.4\times10^{-3}T - 1.55\times10^{-6}T^2 \quad \text{for } (Eu_{0.2}Er_{0.2}Lu_{0.2}Y_{0.2}Yb_{0.2})_2O_3 \tag{12}$$

$$c_{p2} = 123.66 + 13.0\times10^{-3}T - 1.60\times10^{-6}T^2 \quad \text{for } (Sm_{0.2}Er_{0.2}Lu_{0.2}Y_{0.2}Yb_{0.2})_2O_3 \tag{13}$$

Eventually, thermal conductivities of $(Eu_{0.2}Er_{0.2}Lu_{0.2}Y_{0.2}Yb_{0.2})_2O_3$ and $(Sm_{0.2}Er_{0.2}Lu_{0.2}Y_{0.2}Yb_{0.2})_2O_3$ follow the relationship as

$$\kappa_1 = \frac{943.4}{T} + 1.8 \quad \text{for } (Eu_{0.2}Er_{0.2}Lu_{0.2}Y_{0.2}Yb_{0.2})_2O_3 \tag{14}$$

$$\kappa_2 = \frac{787.5}{T} + 2.1 \quad \text{for } (Sm_{0.2}Er_{0.2}Lu_{0.2}Y_{0.2}Yb_{0.2})_2O_3 \tag{15}$$

with R^2 equals to 0.973 and 0.973, respectively. As shown in Fig. 14, the thermal conductivities of HE

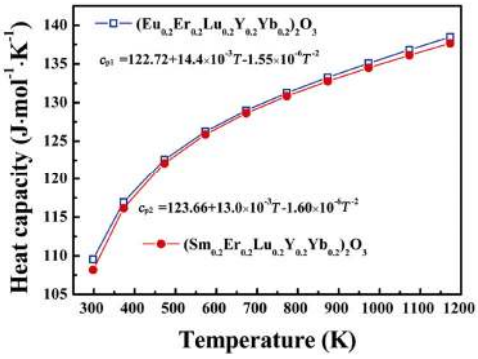

Fig. 13 Heat capacities of $(Eu_{0.2}Er_{0.2}Lu_{0.2}Y_{0.2}Yb_{0.2})_2O_3$ and $(Sm_{0.2}Er_{0.2}Lu_{0.2}Y_{0.2}Yb_{0.2})_2O_3$ calculated from room temperature to 1173 K.

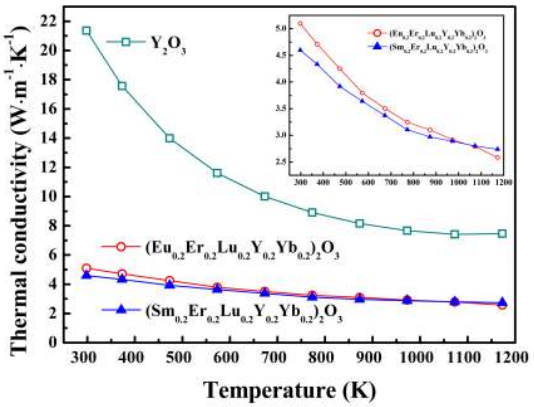

Fig. 14 Thermal conductivities of $(Eu_{0.2}Er_{0.2}Lu_{0.2}Y_{0.2}Yb_{0.2})_2O_3$, $(Sm_{0.2}Er_{0.2}Lu_{0.2}Y_{0.2}Yb_{0.2})_2O_3$, and Y_2O_3 calculated from room temperature to 1173 K.

RE_2O_3 and Y_2O_3 decrease with temperature. More importantly, the thermal conductivities of HE RE_2O_3 within the measured temperature range are evidently lower than that of Y_2O_3. The relatively lower thermal conductivities are caused by a combination of lattice distortion, mass differences of atoms, and composition disorder, as shown in Eqs. (1) and (2). According to the ionic radii of rare earth elements and relative atomic mass that are listed in Table 3, ionic radius difference, which is related to lattice distortion, in $(Eu_{0.2}Er_{0.2}Lu_{0.2}Y_{0.2}Yb_{0.2})_2O_3$ is larger than that in $(Sm_{0.2}Er_{0.2}Lu_{0.2}Y_{0.2}Yb_{0.2})_2O_3$. On the opposite, atomic mass difference in $(Sm_{0.2}Er_{0.2}Lu_{0.2}Y_{0.2}Yb_{0.2})_2O_3$ is higher than that in $(Eu_{0.2}Er_{0.2}Lu_{0.2}Y_{0.2}Yb_{0.2})_2O_3$. In HE RE_2O_3, different RE atoms homogeneously occupy the 8*a* and 24*d* cation sites of the cubic bixbyite structure, leading to severe lattice distortion. Meanwhile, different kinds of atoms bring large mass differences compared with single component Y_2O_3. Low thermal conductivities and close thermal expansion coefficients to Al_2O_3 render HE RE_2O_3 ceramics promising as suitable EBCs for Al_2O_{3f}/Al_2O_3 CMCs to replace Y_2O_3.

3. 5 CMAS resistance

CMAS resistance is a critical requirement for EBC coatings. In this work, CMAS corrosion resistance of bulk $(Eu_{0.2}Er_{0.2}Lu_{0.2}Y_{0.2}Yb_{0.2})_2O_3$ and $(Sm_{0.2}Er_{0.2}Lu_{0.2}Y_{0.2}Yb_{0.2})_2O_3$ ceramics was tested at 1250 and 1350 ℃ for up to 4 h and the cross-sectional morphologies are shown in Fig. 15. One can find that the cross-sections of bulk $(Eu_{0.2}Er_{0.2}Lu_{0.2}Y_{0.2}Yb_{0.2})_2O_3$ and $(Sm_{0.2}Er_{0.2}Lu_{0.2}Y_{0.2}Yb_{0.2})_2O_3$ after CMAS attack are quite similar, presenting a triple-layer structure, i.e., the CMAS layer, a transition layer, and the HE RE_2O_3 substrate layer

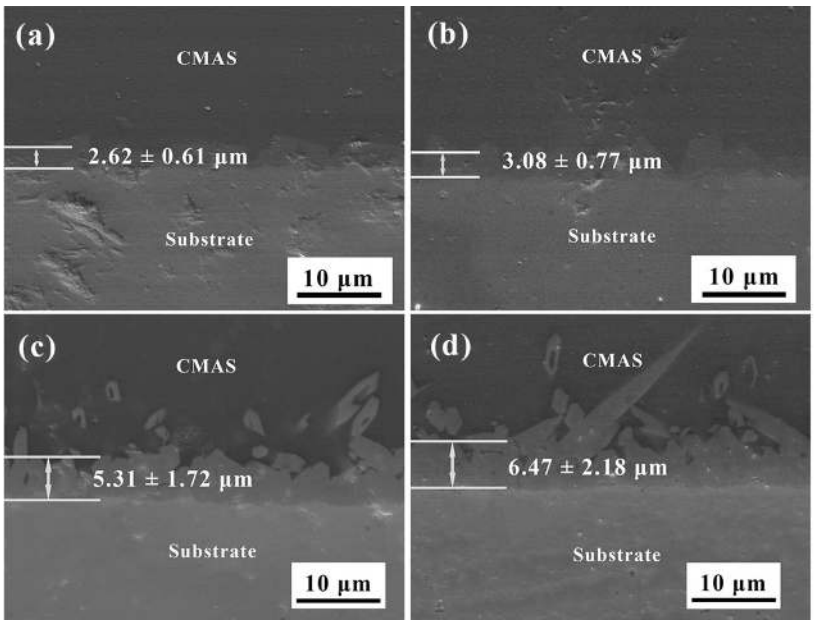

Fig. 15 Cross-section morphologies of (a, c) $(Eu_{0.2}Er_{0.2}Lu_{0.2}Y_{0.2}Yb_{0.2})_2O_3$ and (b, d) $(Sm_{0.2}Er_{0.2}Lu_{0.2}Y_{0.2}Yb_{0.2})_2O_3$ attacked by CMAS at 1250 and 1350 ℃ for 4 h.

from top to bottom. As shown in Figs. 15(a) and 15(b), after CMAS corrosion at 1250 ℃ for 4 h, there is only a smooth reaction layer between the CMAS layer and the HE RE_2O_3 substrate layer, which are 2.62±0.61 and 3.08±0.77 μm, respectively. When the corrosion temperature increases to 1350 ℃, it can be observed from Figs. 15(c) and 15(d) that the reaction layers turned to be rugged with burrs. The visible reaction layers increase to about 5.31±1.72 and 6.47±2.18 μm, respectively. Meanwhile, the substrates of HE RE_2O_3 ceramics still remain relatively glossy without pores or cracks caused by CMAS attack. The morphology integrity of the attacked HE RE_2O_3 ceramics indicate their better CMAS resistance than Y_2O_3 [22], YSZ [22, 62], $REPO_4$ (RE = Nd, Sm, Gd) [62], Ba_2REAlO_5 (RE = Yb, Er, Dy) [63], and high-entropy $RE_2Si_2O_7$ [64].

Table 7 compares the thicknesses of the reaction layers of several common TBC/EBC materials that are attacked by CMAS under different conditions. After being corroded at 1250 ℃ for 4 h, thickness values of the reaction layers upon the CMAS deposited $(Eu_{0.2}Er_{0.2}Lu_{0.2}Y_{0.2}Yb_{0.2})_2O_3$ and $(Sm_{0.2}Er_{0.2}Lu_{0.2}Y_{0.2}Yb_{0.2})_2O_3$ ceramics (with a concentration of about 77 mg/cm^2) are only 2.62±0.61 and 3.08±0.77 μm, which are less than a half of the values in $REPO_4$ (RE = Nd, Sm, Gd) [62] and Ba_2REAlO_5 (RE = Yb, Er, Dy) [63] (with a concentration of about 15 mg/cm^2). After being corroded at 1250 ℃ for 1 h, MOCVD YSZ coating possessed a 5 μm-thick reaction layer while YSZ pellet infiltrated by CMAS for 4 h has a reaction layer with a depth of 50 μm.

Table 7 Thickness of the reaction layers of several thermal/environmental barrier coating materials after CMAS attack under different conditions

Material	Temperature and duration	CMAS composite	CMAS loading and loading methods	Thickness of reaction layers
MOCVD Y_2O_3 coating [22]	1250 ℃, 1 h	35.3CaO–9.6MgO–6.9Al_2O_3–48.2SiO_2	30 mg/cm^2 by powder depositing	30 μm
MOCVD YSZ coating [22]	1250 ℃, 1 h	35.3CaO–9.6MgO–6.9Al_2O_3–48.2SiO_2	30 mg/cm^2 by powder depositing	5 μm
YSZ pellet [62]	1250 ℃, 4 h	22CaO–19MgO–15$AlO_{1.5}$–44SiO_2	15 mg/cm^2 by suspension dropping	~50 μm
$LnPO_4$ pellets [62]	1250 ℃, 4 h	22CaO–19MgO–15$AlO_{1.5}$–44SiO_2	15 mg/cm^2 by suspension dropping	10–15 μm
Ba_2REAlO_5 pellets [63]	1250 ℃, 4 h	22CaO–19MgO–14$AlO_{1.5}$–45SiO_2	~15 mg/cm^2 by slurry dropping	10–15 μm
High-entropy $RE_2Si_2O_7$ [64]	1500 ℃, 4 and 50 h	33CaO–9MgO–13$AlO_{1.5}$–45SiO_2	30 mg/cm^2 by suspension coating	~300 μm
High-entropy RE_2O_3 (this work)	1250 ℃, 4 h	22CaO–19MgO–14$AlO_{1.5}$–45SiO_2	~77 mg/cm^2 by slurry dropping	2.62±0.61 μm, 3.08±0.77 μm
High-entropy RE_2O_3 (this work)	1350 ℃, 4 h	22CaO–19MgO–14$AlO_{1.5}$–45SiO_2	~77 mg/cm^2 by slurry dropping	5.31±1.72 μm, 6.47±2.18 μm

EDS linear scanning along the white lines in Fig. 16 displays the relative amount of constituting elements from CMAS to HE RE_2O_3 that were heated at 1350 ℃ for 4 h. The undulate distributions of elements match with the changes of morphologies which could be distinguished by colors. Mg and Al have infiltrated into HE RE_2O_3 substrates largely, leaving Si behind them, while Ca remains mostly in the CMAS layer. As for rare earth elements, Y seems to be eagerly to climb upward while the other four elements are similar and remain mostly in the substrates of HE RE_2O_3. To figure out the reaction mechanism, samples half-coated by CMAS were designed as shown in Fig. 17(a). In Figs. 17(b) and 17(c), a step appears at the transition zone of each sample, revealing that the reaction mechanism is characterized by the diffusion from CMAS to HE RE_2O_3.

Figure 18 presents the XRD patterns of the surfaces of HE RE_2O_3 after CMAS attack at 1250 ℃ for 1, 2, and 4 h, and at 1350 ℃ for 4 h, corresponding to curves (2)–(5), respectively. In Fig. 18(a), wherein HE $(Eu_{0.2}Er_{0.2}Lu_{0.2}Y_{0.2}Yb_{0.2})_2O_3$ was attacked by CMAS, the only phase that could be identified was $CaSiO_3$ (in $P2_1/a$ space group), even though the as-marked $CaSiO_3$ phase only matches the position with a shift to lower angle. In detail, curves (2) and (3) are similar despite a new strong peak at $2\theta \approx 37°$ appears in curve (3), which also exists in curve (4). However, most of the peaks still remain unknown, demonstrating that the phase compositions of the surface of $(Sm_{0.2}Er_{0.2}Lu_{0.2}Y_{0.2}Yb_{0.2})_2O_3$ after CMAS attack are more complex.

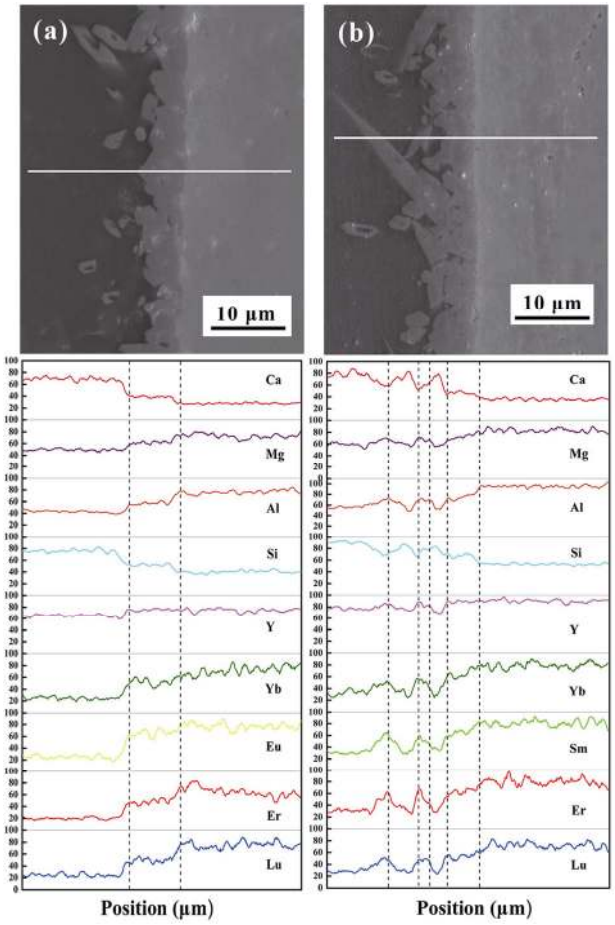

Fig. 16 Relative amount of constituting elements in CMAS and HE RE_2O_3 substrates: (a) $(Eu_{0.2}Er_{0.2}Lu_{0.2}Y_{0.2}Yb_{0.2})_2O_3$ and (b) $(Sm_{0.2}Er_{0.2}Lu_{0.2}Y_{0.2}Yb_{0.2})_2O_3$ after CMAS attack at 1350 ℃ for 4 h.

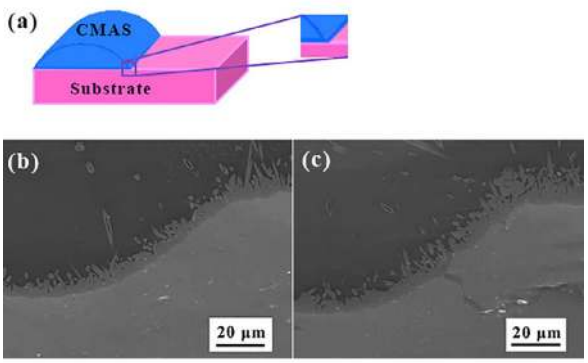

Fig. 17 (a) Schematic diagram of the designed half-coated sample, and SEM images of the transition zone of (b) $(Eu_{0.2}Er_{0.2}Lu_{0.2}Y_{0.2}Yb_{0.2})_2O_3$ and (c) $(Sm_{0.2}Er_{0.2}Lu_{0.2}Y_{0.2}Yb_{0.2})_2O_3$, demonstrating the reaction occurs on the HE RE_2O_3 side through CMAS attack.

In order to identify the compositions of reaction products on the CMAS attacked surfaces of HE RE_2O_3 ceramics, powders of CMAS and HE RE_2O_3 were mixed with a mass ratio of 1:2 and then heated at 1350 ℃ for 4 h. The XRD patterns of $(Eu_{0.2}Er_{0.2}Lu_{0.2}Y_{0.2}Yb_{0.2})_2O_3$ and $(Sm_{0.2}Er_{0.2}Lu_{0.2}Y_{0.2}Yb_{0.2})_2O_3$ powders after reaction with CMAS powders are shown in Fig. 19, wherein rare earth aluminate $RE_3Al_5O_{12}$, $Ca_2(SiO_4)$, and $Ca_2RE_8O(SiO_4)_6$ oxyapatites [65,66] are identified. However, XRD patterns of these three phases cannot match any of the unknown peaks in Fig. 18. The mismatch between XRD patterns in Fig. 18 and Fig. 19 might be related to reaction methods. The XRD patterns shown in Fig. 19 are from the reaction of $(Eu_{0.2}Er_{0.2}Lu_{0.2}Y_{0.2}Yb_{0.2})_2O_3$ and $(Sm_{0.2}Er_{0.2}Lu_{0.2}Y_{0.2}Yb_{0.2})_2O_3$ powders with CMAS powders, while the XRD patterns shown in Fig. 18 are from reaction of the surfaces of bulk $(Eu_{0.2}Er_{0.2}Lu_{0.2}Y_{0.2}Yb_{0.2})_2O_3$ and $(Sm_{0.2}Er_{0.2}Lu_{0.2}Y_{0.2}Yb_{0.2})_2O_3$ with CMAS. For powder reaction, the reactants were well-mixed. As a result, the reaction was sufficient. While for the surface attack, it can be seen from Fig. 16 that the relative amounts of

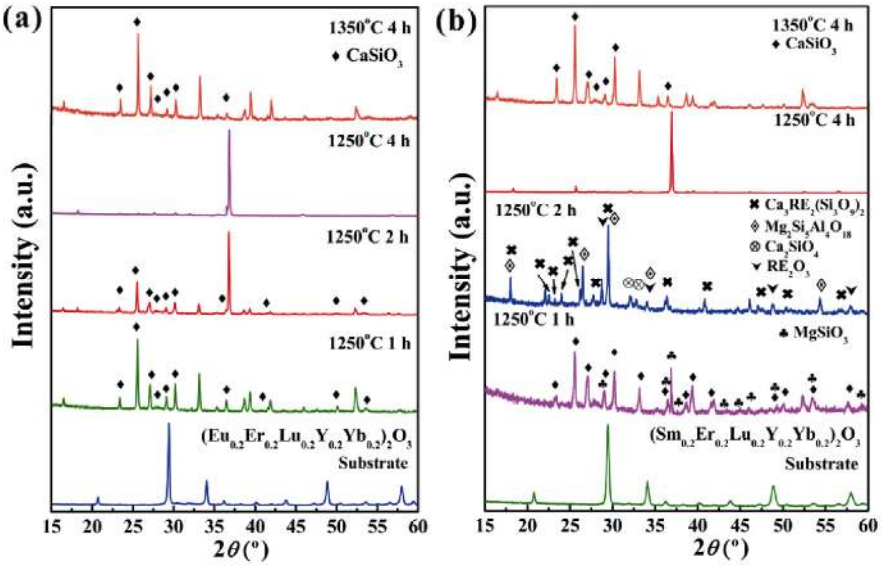

Fig. 18 XRD patterns of the surfaces of bulk (a) $(Eu_{0.2}Er_{0.2}Lu_{0.2}Y_{0.2}Yb_{0.2})_2O_3$ and (b) $(Sm_{0.2}Er_{0.2}Lu_{0.2}Y_{0.2}Yb_{0.2})_2O_3$ after CMAS attack at 1250 ℃ for 1, 2, and 4 h and at 1350 ℃ for 4 h.

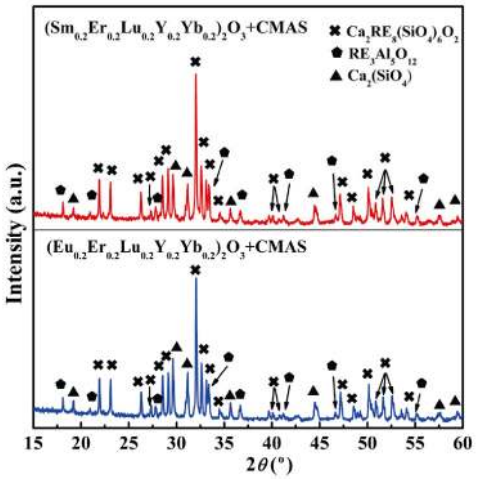

Fig. 19 XRD patterns of the $(Eu_{0.2}Er_{0.2}Lu_{0.2}Y_{0.2}Yb_{0.2})_2O_3$ and $(Sm_{0.2}Er_{0.2}Lu_{0.2}Y_{0.2}Yb_{0.2})_2O_3$ powders after reacting with CMAS powders at 1350 ℃ for 4 h.

constituting elements in CMAS that permeated into HE RE_2O_3 substrates are different. The rapid diffusion of Mg and Al than other elements towards HE RE_2O_3 may cause the reaction products on the surface different from those of powder reaction. Furthermore, the CMAS loading on HE RE_2O_3 is about 0.77 mg/cm^2, which is more than four times thicker than that on $REPO_4$ (RE = Nd, Sm, Gd) [62] and Ba_2REAlO_5 (RE = Yb, Er, Dy) [63] (with a concentration of about 15 mg/cm^2). Thus, the XRD patterns from the surfaces of HE RE_2O_3 are different from those on $REPO_4$ (RE = Nd, Sm, Gd) and Ba_2REAlO_5 (RE = Yb, Er, Dy) and also from those of powder reactions.

4 Conclusions

In this study, four cubic bixbyite structured high-entropy rare earth oxides, including $(Eu_{0.2}Er_{0.2}Lu_{0.2}Y_{0.2}Yb_{0.2})_2O_3$, $(Sm_{0.2}Er_{0.2}Lu_{0.2}Y_{0.2}Yb_{0.2})_2O_3$, $(Sm_{0.2}Eu_{0.2}Er_{0.2}Y_{0.2}Yb_{0.2})_2O_3$, and $(Sm_{0.2}Eu_{0.2}Lu_{0.2}Y_{0.2}Yb_{0.2})_2O_3$ were designed and successfully synthesized using a solid state reaction method. And bulk $(Eu_{0.2}Er_{0.2}Lu_{0.2}Y_{0.2}Yb_{0.2})_2O_3$ and $(Sm_{0.2}Er_{0.2}Lu_{0.2}Y_{0.2}Yb_{0.2})_2O_3$ ceramics were prepared via spark plasma sintering. The densities of bulk $(Eu_{0.2}Er_{0.2}Lu_{0.2}Y_{0.2}Yb_{0.2})_2O_3$ and $(Sm_{0.2}Er_{0.2}Lu_{0.2}Y_{0.2}Yb_{0.2})_2O_3$ ceramics are 7.88 and 7.82 g/cm^3, respectively. The HE RE_2O_3 ceramics crystallize in cubic bixbyite structure with an $Ia\bar{3}$ space group despite the fact that one of the raw materials, i.e., Sm_2O_3, is in monoclinic structure with a $C2/m$ space group, which proves that materials with different crystal structures can be integrated into a high symmetry structure through entropy stabilization. $(Eu_{0.2}Er_{0.2}Lu_{0.2}Y_{0.2}Yb_{0.2})_2O_3$ and $(Sm_{0.2}Er_{0.2}Lu_{0.2}Y_{0.2}Yb_{0.2})_2O_3$ exhibit close mechanical properties and superior thermal properties to Y_2O_3. It is worth highlighting that the room temperature thermal conductivities of $(Eu_{0.2}Er_{0.2}Lu_{0.2}Y_{0.2}Yb_{0.2})_2O_3$ and $(Sm_{0.2}Er_{0.2}Lu_{0.2}Y_{0.2}Yb_{0.2})_2O_3$ are 5.1 and 4.6 $W\cdot m^{-1}\cdot K^{-1}$, respectively, which are only about 23.8% and 21.5% of that of Y_2O_3 (21.4 $W\cdot m^{-1}\cdot K^{-1}$). More importantly, high-entropy $(Eu_{0.2}Er_{0.2}Lu_{0.2}Y_{0.2}Yb_{0.2})_2O_3$ and $(Sm_{0.2}Er_{0.2}Lu_{0.2}Y_{0.2}Yb_{0.2})_2O_3$ ceramics have good CMAS resistance. After attacking by CMAS at 1350 ℃ for 4 h, the thicknesses of the reaction layers are only 5.31±1.72

and 6.47±2.18 μm, respectively, and the HE RE_2O_3 substrates still remain pore-free and crack-free. Close mechanical properties to Y_2O_3, low thermal conductivities, close thermal expansion coefficient to Y_2O_3 and Al_2O_3, and good CMAS resistance indicate that $(Eu_{0.2}Er_{0.2}Lu_{0.2}Y_{0.2}Yb_{0.2})_2O_3$ and $(Sm_{0.2}Er_{0.2}Lu_{0.2}Y_{0.2}Yb_{0.2})_2O_3$ are promising EBC materials for Al_2O_{3f}/Al_2O_3 CMCs. However, we must acknowledge that high-entropy $(Eu_{0.2}Er_{0.2}Lu_{0.2}Y_{0.2}Yb_{0.2})_2O_3$ and $(Sm_{0.2}Er_{0.2}Lu_{0.2}Y_{0.2}Yb_{0.2})_2O_3$ ceramics are more brittle than Y_2O_3, which needs further attention in other high-entropy ceramics.

Acknowledgements

This work was financially supported by the National Natural Science Foundation of China under Grant Nos. 51972089, 51672064, and U1637210.

References

[1] Mechnich P, Braue W. Air plasma-sprayed Y_2O_3 coatings for Al_2O_{3f}/Al_2O_3 ceramic matrix composites. *J Eur Ceram Soc* 2013, **33**: 2645–2653.

[2] Tressler RE. Recent developments in fibers and interphases for high temperature ceramic matrix composites. *Compos Part A: Appl Sci Manuf* 1999, **30**: 429–437.

[3] Ohnabe H, Masaki S, Onozuka M, *et al*. Potential application of ceramic matrix composites to aero-engine components. *Compos Part A: Appl Sci Manuf* 1999, **30**: 489–496.

[4] Richards BT, Wadley HNG. Plasma spray deposition of tri-layer environmental barrier coatings. *J Eur Ceram Soc* 2014, **34**: 3069–3083.

[5] Zawada LP, Hay RS, Lee SS, *et al*. Characterization and high-temperature mechanical behavior of an oxide/oxide composite. *J Am Ceram Soc* 2003, **86**: 981–990.

[6] Wilson DM, Visser LR. High performance oxide fibers for metal and ceramic composites. *Compos Part A: Appl Sci Manuf* 2001, **32**: 1143–1153.

[7] Dong Y, Ren K, Lu YH, *et al*. High-entropy environmental barrier coating for the ceramic matrix composites. *J Eur Ceram Soc* 2019, **39**: 2574–2579.

[8] Naslain R. Recent advances in the field of ceramic fibers and ceramic matrix composites. *J Phys IV France* 2005, **123**: 3–17.

[9] Opila EJ, Myers DL. Alumina volatility in water vapor at elevated temperatures. *J Am Ceram Soc* 2004, **87**: 1701–1705.

[10] Rai AK, Bhattacharya RS, Wolfe DE, *et al*. CMAS-resistant thermal barrier coatings (TBC). *Int J Appl Ceram Technol* 2010, **7**: 662–674.

[11] Levi CG, Hutchinson JW, Vidal-Sétif MH, *et al*. Environmental degradation of thermal-barrier coatings by molten deposits. *MRS Bull* 2012, **37**: 932–941.

[12] Wiesner VL, Harder BJ, Bansal NP. High-temperature interactions of desert sand CMAS glass with yttrium disilicate environmental barrier coating material. *Ceram Int* 2018, **44**: 22738–22743.

[13] Grant KM, Krämer S, Löfvander JPA, *et al*. CMAS degradation of environmental barrier coatings. *Surf Coat Technol* 2007, **202**: 653–657.

[14] Harder BJ, Ramìrez-Rico J, Almer JD, *et al*. Chemical and mechanical consequences of environmental barrier coating exposure to calcium-magnesium-aluminosilicate. *J Am Ceram Soc* 2011, **94**: s178–s185.

[15] Kitamura J, Tang ZL, Mizuno H, *et al*. Structural, mechanical and erosion properties of yttrium oxide coatings by axial suspension plasma spraying for electronics applications. *J Therm Spray Technol* 2011, **20**: 170–185.

[16] Harada Y, Suzuki T, Hirano K, *et al*. Environmental effects on ultra-high temperature creep behavior of directionally solidified oxide eutectic ceramics. *J Eur Ceram Soc* 2005, **25**: 1275–1283.

[17] Zhao ZF, Chen H, Xiang HM, *et al*. High-entropy $(Y_{0.2}Nd_{0.2}Sm_{0.2}Eu_{0.2}Er_{0.2})AlO_3$: A promising thermal/environmental barrier material for oxide/oxide composites. *J Mater Sci Technol* 2020, **47**: 45–51.

[18] Wu P, Pelton AD. Coupled thermodynamic-phase diagram assessment of the rare earth oxide-aluminium oxide binary systems. *J Alloys Compd* 1992, **179**: 259–287.

[19] Nielsen TH, Leipold MH. Thermal expansion of yttrium oxide and of magnesium oxide with yttrium oxide. *J Am Ceram Soc* 1964, **47**: 256.

[20] Curtis CE. Properties of yttrium oxide ceramics. *J Am Ceram Soc* 1957, **40**: 274–278.

[21] Gatzen C, Mack DE, Guillon O, *et al*. $YAlO_3$—A novel environmental barrier coating for Al_2O_3/Al_2O_3–ceramic matrix composites. *Coatings* 2019, **9**: 609.

[22] Eils NK, Mechnich P, Braue W. Effect of CMAS deposits on MOCVD coatings in the system Y_2O_3–ZrO_2: Phase relationships. *J Am Ceram Soc* 2013, **96**: 3333–3340.

[23] Rost CM, Sachet E, Borman T, *et al*. Entropy-stabilized oxides. *Nat Commun* 2015, **6**: 8485.

[24] Zhang Y, Zuo TT, Tang Z, *et al*. Microstructures and properties of high-entropy alloys. *Prog Mater Sci* 2014, **61**: 1–93.

[25] Chen KP, Pei XT, Tang L, *et al*. A five-component entropy-stabilized fluorite oxide. *J Eur Ceram Soc* 2018, **38**: 4161–4164.

[26] Qin Y, Liu JX, Li F, *et al*. A high entropy silicide by reactive spark plasma sintering. *J Adv Ceram* 2019, **8**: 148–152.

[27] Dong Y, Ren K, Lu YH, *et al*. High-entropy environmental barrier coating for the ceramic matrix composites. *J Eur Ceram Soc* 2019, **39**: 2574–2579.

[28] Braun JL, Rost CM, Lim M, *et al*. Charge-induced disorder controls the thermal conductivity of entropy-stabilized

oxides. *Adv Mater* 2018, **30**: 1805004.
[29] Zhao ZF, Chen H, Xiang HM, *et al*. High entropy defective fluorite structured rare-earth niobates and tantalates for thermal barrier applications. *J Adv Ceram* 2020, **9**: 303–311.
[30] Chen H, Zhao ZF, Xiang HM, *et al*. High entropy $(Y_{0.2}Yb_{0.2}Lu_{0.2}Eu_{0.2}Er_{0.2})_3Al_5O_{12}$: A novel high temperature stable thermal barrier material. *J Mater Sci Technol* 2020, **48**: 57–62.
[31] Zhao ZF, Xiang HM, Chen H, *et al*. High-entropy $(Nd_{0.2}Sm_{0.2}Eu_{0.2}Y_{0.2}Yb_{0.2})_4Al_2O_9$ with good high temperature stability, low thermal conductivity, and anisotropic thermal expansivity. *J Adv Ceram* 2020, **9**: 595–605.
[32] Chen H, Xiang HM, Dai FZ, *et al*. High entropy $(Yb_{0.25}Y_{0.25}Lu_{0.25}Er_{0.25})_2SiO_5$ with strong anisotropy in thermal expansion. *J Mater Sci Technol* 2020, **36**: 134–139.
[33] Zhao ZF, Xiang HM, Dai FZ, *et al*. $(La_{0.2}Ce_{0.2}Nd_{0.2}Sm_{0.2}Eu_{0.2})_2Zr_2O_7$: A novel high-entropy ceramic with low thermal conductivity and sluggish grain growth rate. *J Mater Sci Technol* 2019, **35**: 2647–2651.
[34] Sarkar A, Loho C, Velasco L, *et al*. Multicomponent equiatomic rare earth oxides with a narrow band gap and associated praseodymium multivalency. *Dalton Trans* 2017, **46**: 12167–12176.
[35] Gild J, Zhang Y, Harrington T, *et al*. High-entropy metal diborides: A new class of high-entropy materials and a new type of ultrahigh temperature ceramics. *Sci Rep* 2016, **6**: 37946.
[36] Anand G, Wynn AP, Handley CM, *et al*. Phase stability and distortion in high-entropy oxides. *Acta Mater* 2018, **146**: 119–125.
[37] Lu K, Liu JX, Wei XF, *et al*. Microstructures and mechanical properties of high-entropy $(Ti_{0.2}Zr_{0.2}Hf_{0.2}Nb_{0.2}Ta_{0.2})C$ ceramics with the addition of SiC secondary phase. *J Eur Ceram Soc* 2020, **40**: 1839–1847.
[38] Toberer ES, Zevalkink A, Snyder GJ. Phonon engineering through crystal chemistry. *J Mater Chem* 2011, **21**: 15843.
[39] Zhou X, Liu D, Bu HL, *et al*. XRD-based quantitative analysis of clay minerals using reference intensity ratios, mineral intensity factors, Rietveld, and full pattern summation methods: A critical review. *Solid Earth Sci* 2018, **3**: 16–29.
[40] Le Saoût G, Kocaba V, Scrivener K. Application of the Rietveld method to the analysis of anhydrous cement. *Cem Concr Res* 2011, **41**: 133–148.
[41] Collins TJ. ImageJ for microscopy. *BioTechniques* 2007, **43**: S25–S30.
[42] Bao YW, Liu LZ, Zhou YC. Assessing the elastic parameters and energy-dissipation capacity of solid materials: A residual indent may tell all. *Acta Mater* 2005, **53**: 4857–4862.
[43] Wang F, Guo L, Wang CM, *et al*. Calcium-magnesium-alumina-silicate (CMAS) resistance characteristics of $LnPO_4$ (Ln = Nd, Sm, Gd) thermal barrier oxides. *J Eur Ceram Soc* 2017, **37**: 289–296.
[44] Wu B, Zinkevich M, Aldinger F, *et al*. Ab initio study on structure and phase transition of A- and B-type rare-earth sesquioxides Ln_2O_3 (Ln = La–Lu, Y, and Sc) based on density function theory. *J Solid State Chem* 2007, **180**: 3280–3287.
[45] Atou T, Kusaba K, Tsuchida Y, *et al*. Reversible B-type–A-type transition of Sm_2O_3 under high pressure. *Mater Res Bull* 1989, **24**: 1171–1176.
[46] Zhang YM, Jung IH. Critical evaluation of thermodynamic properties of rare earth sesquioxides (RE = La, Ce, Pr, Nd, Pm, Sm, Eu, Gd, Tb, Dy, Ho, Er, Tm, Yb, Lu, Sc and Y). *Calphad* 2017, **58**: 169–203.
[47] Roth RS, Schneider SJ. Phase equilibria in systems involving the rare-earth oxides. Part I. Polymorphism of the oxides of the trivalent rare-earth ions. *J Res Natl Bureau Stand Sect A: Phys Chem* 1960, **64A**: 309–316.
[48] Shevthenko AV, Lopato LM. DTA method applikation to the highest refractory oxide systems investigation. *Thermochimica Acta* 1985, **93**: 537–540.
[49] Warshaw I, Roy R. Polymorphism of the rare earth sesquioxides1. *J Phys Chem* 1961, **65**: 2048–2051.
[50] Zinkevich M. Thermodynamics of rare earth sesquioxides. *Prog Mater Sci* 2007, **52**: 597–647.
[51] Curtis CE, Tharp AG. Ceramic properties of europium oxide. *J Am Ceram Soc* 1959, **42**: 151.
[52] Foex M, Traverse JP. Investigations about crystalline trasformation in rare earths sesquioxides at high temperatures. 1966, **3**: 429–453.
[53] Stecura S, Campbell WJ. Thermal expansion and phase inversion of rare-earth oxides. Office of Scientific and Technical Information (OSTI), 1960.
[54] Schleid T, Meyer G. Single crystals of rare earth oxides from reducing halide melts. *J Less-Common Metals* 1989, **149**: 73–80.
[55] Tseng KP, Yang Q, McCormack SJ, *et al*. High-entropy, phase-constrained, lanthanide sesquioxide. *J Am Ceram Soc* 2020, **103**: 569–576.
[56] Bünzli JG, Mcgill I. *Rare Earth Elements*. Ullmann's Encyclopedia of Industrial Chemistry, 2018.
[57] Ahmadi B, Reza SR, Ahsanzadeh-Vadeqani M, *et al*. Mechanical and optical properties of spark plasma sintered transparent Y_2O_3 ceramics. *Ceram Int* 2016, **42**: 17081–17088.
[58] Boccaccini AR. Machinability and brittleness of glass-ceramics. *J Mater Process Technol* 1997, **65**: 302–304.
[59] Bao YW, Hu CF, Zhou YC. Damage tolerance of nanolayer grained ceramics and quantitative estimation. *Mater Sci Technol* 2006, **22**: 227–230.
[60] Zhou YC, Lu XP, Xiang HM, *et al*. Preparation, mechanical, and thermal properties of a promising thermal barrier material: $Y_4Al_2O_9$. *J Adv Ceram* 2015, **4**: 94–102.
[61] Zhang SY, Li HL, Zhou SH, *et al*. Estimation thermal expansion coefficient from lattice energy for inorganic crystals. *Jpn J Appl Phys* 2006, **45**: 8801–8804.
[62] Wang F, Guo L, Wang CM, *et al*. Calcium-magnesium-alumina-silicate (CMAS) resistance characteristics of $LnPO_4$ (Ln = Nd, Sm, Gd) thermal barrier oxides. *J Eur Ceram Soc* 2017, **37**: 289–296.
[63] Wei LL, Guo L, Li MZ, *et al*. Calcium-magnesium-

alumina-silicate (CMAS) resistant Ba_2REAlO_5 (RE = Yb, Er, Dy) ceramics for thermal barrier coatings. *J Eur Ceram Soc* 2017, **37**: 4991–5000.

[64] Sun LC, Luo YX, Tian ZL, *et al*. High temperature corrosion of $(Er_{0.25}Tm_{0.25}Yb_{0.25}Lu_{0.25})_2Si_2O_7$ environmental barrier coating material subjected to water vapor and molten calcium-magnesium-aluminosilicate (CMAS). *Corros Sci* 2020, **175**: 108881.

[65] Crum JV, Chong S, Peterson JA, *et al*. Syntheses, crystal structures, and comparisons of rare-earth oxyapatites $Ca_2RE_8(SiO_4)_6O_2$ (RE = La, Nd, Sm, Eu, or Yb) and $NaLa_9(SiO_4)_6O_2$. *Acta Cryst E* 2019, **75**: 1020–1025.

[66] Costa G, Harder BJ, Bansal NP, *et al*. Thermochemistry of calcium rare-earth silicate oxyapatites. *J Am Ceram Soc* 2020, **103**: 1446–1453.